Article

Unveiling the Mechanisms of EGCG−p53 Interactions through Molecular Dynamics Simulations

Erick Bahena Culhuac and Martiniano Bello*

Cite This: *ACS Omega* 2024, 9, 20066−20085

Read Online

ACCESS | Metrics & More | Article Recommendations | SI Supporting Information

ABSTRACT: Green tea consumption is associated with protective and preventive effects against various types of cancer. These effects are attributed to polyphenols, particularly epigallocatechin-3-gallate (EGCG). EGCG acts by directly inhibiting tumor suppressor protein p53. The binding mechanism by which EGCG inhibits p53 activity is associated with residues Trp23−Lys24 and Pro47−Thr55 within the p53 N-terminal domain (NTD). However, the structural and thermodynamic aspects of the interaction between EGCG and p53 are poorly understood. Therefore, based on crystallographic data, we combine docking, molecular dynamics (MD) simulations, and molecular mechanics generalized Born surface area approaches to explore the intricacies of the EGCG−p53 binding mechanism. A triplicate microsecond MD simulation for each system is initially performed to capture diverse p53 NTD conformations. From the start, the most populated cluster of the second run (R2−1) stands out due to a unique opening between Trp23 and Trp53. During MD simulations, this conformation allows EGCG to sustain a high level of stability and affinity while interacting with both regions of interest and deepening the binding pocket. Structural analysis emphasizes the significance of pyrogallol motifs in EGCG binding. Therefore, the conformational shift in this gap is pivotal, enabling EGCG to impede p53 interactions and manifest its anticancer properties. These findings enhance the present comprehension of the anticancer properties of green tea polyphenols and pave the way for future therapeutic developments.
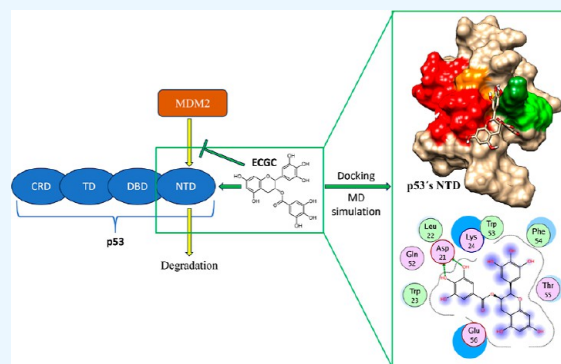
1. INTRODUCTION

Different epidemiologic studies have reported that green tea drinking has protective and preventive effects against several types of cancer, such as breast, colon, lung, and prostate cancers.[1−5] The chemoprotective effects of green tea have been attributed to polyphenol epigallocatechin-3-gallate (EGCG), which is its most abundant (50−80%) and active compound.[3,6] Previous studies have indicated that there are multiple signaling pathways associated with the antitumor activity of EGCG,[1,7,8] such as suppression of various protein kinases,[9−11] disruption of the activation of transcription factors such as EGFR and NF-κB,[12−14] and inhibition of cell migration and metastasis.[15−19]

The TP53 gene encodes the p53 tumor suppressor protein.[20] This protein is commonly referred to as the guardian of the genome because it plays a vital role in multicellular organisms by regulating the cell cycle, where it promotes cell apoptosis by maintaining DNA stability and impeding tumor suppression.[21−24] When a cell is damaged, the p53 protein evaluates the degree of DNA damage and promotes cellular repair if it is not significant; otherwise, the protein causes cell apoptosis.

Under normal conditions, p53 is an unstable protein present at low concentrations in the cell and has a short half-life (approximately 20 min) due to constant ubiquitylation and degradation by the mouse double minute 2 (MDM2) homologue.[25] Under stress conditions such as DNA damage

or UV radiation, the degradation of p53 is suppressed by avoiding ubiquitylation, allowing extended P53 half-life and promoting its stabilization and activation.[26−28]

The high concentration of p53 in the nucleus switches on gene expression, activating cell-cycle arrest, apoptosis, and DNA-repair events.[29] In addition, although p53 is mainly present in the nucleus, p53 can translocate to the cytoplasm and mitochondria and act directly on some antiapoptotic proteins.[30,31]

The active state of the p53 protein is a tetramer in which 393 amino acids comprise each subunit. Each subunit has several domains: the N-terminal domain (NTD), a DNA-binding domain (DBD), a tetramerization domain (TD), and a C-terminal regulatory domain (CRD).[32] NTD is an intrinsically disordered protein formed by three domains: two trans-activation domains (TADI and TADII) and a proline-rich domain (PD). TADI and TADII are localized between residues
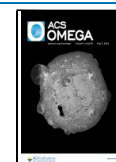
1−42 and 43−62, respectively, which are regulator regions of p53 because they represent binding regions for the transcriptional machinery and the association of MDM2 that participates in the ubiquitylation of p53. DBD is localized between residues 102 and 292 and is essential for the transcriptional activity of p53. TD spans amino acids 324 to 355 and participates in the formation of a protein−protein interface to create a p53 tetramer.[33] CRD is a highly conserved region essential for the nuclear exportation of p53.[34]

Previous studies have shown that EGCG affects the level of p53 expression in different types of cancer.[35−38] The antitumor effects of EGCG on cancer cell lines have been attributed to its disruption of the interaction between p53 and MDM2.[36,39] It has also been reported that EGCG promotes the stabilization of p53 through the phosphorylation of punctual serine residues.[36]

A recent study combining experimental and theoretical approaches demonstrated that there is direct binding between EGCG and p53 and revealed that the binding mechanism is localized at the NTD of p53.[40] However, the structural and thermodynamic basis of the molecular recognition mechanism between EGCG and P53 is poorly understood.

Intrinsically disordered proteins, such as the NTD region of p53, lack well-defined secondary or tertiary structure until they bind to other molecules.[41] Consequently, molecular dynamics (MD) simulations offer a promising avenue to comprehend the intricacies of their behavior. Moreover, establishing binding pockets and conformational changes based on MD simulations has been a widely used strategy.[42−45] Therefore, in this work, we take advantage of the crystallographic data available and combine docking and MD simulations on the microsecond scale with the molecular mechanics generalized Born surface area (MMGBSA) approach to explore the structural and thermodynamic basis of the binding between EGCG and p53.

2. METHODS

2.1. Construction of the Systems.
Structures of p53 were taken from the complex between the CBP nuclear coactivator binding domain and p53 (PDB entry 2L14). PDB 2L14 was meticulously selected for its integrity, containing Trp23 and Trp53 without mutations. Notably, it was chosen over other options due to the presence of α-helices, a structure characteristic widely reported in NTD.[46] The crystallographic p53 structure was submitted to triplicate MD simulations in the microsecond (μs) time scale to obtain equilibrated p53 conformations. Of these simulations, the first, second, and third most populated conformers were obtained through a clustering analysis for use as starting conformations to indicate the binding mode between EGCG and critical amino acids of the p53 surface. ECGC conformations were selected based on the most favorable interactions observed with the critical residues during directed docking. Specifically, for the R1−3, R2−1, and R3−2 systems, Autodock4 was employed, whereas in the R3−1 and R3−3 systems, Swissdock server was employed. The p53− EGCG complexes were constructed in Amber22 package[47] using antechamber and tleap modules. Ligand force field were constructed considering general amber force field (GAFF)[48] and AM1-BCC atomic charges.[49] P53 was modeled with the AMBER99SB-ILDN force field,[50] a suitable force field to study proteins containing intrinsically disordered regions such as p53.[51] Solvation and neutralization of systems were as follows: they were solvated in a truncated octahedral water box of 12 Å dimension[52] and neutralized with a salt concentration of 0.15 M of NaCl.

2.2. Minimization and Molecular Dynamics Studies.
P53 and p53−EGCG complexes were minimized considering 5000 circles of steepest descent and 5000 cycles of conjugate gradient method. Systems were heated from 0 to 310 K over 200 ps under an *NVT* ensemble, whereas heavy receptor atoms were constrained with an elastic constant of 3 kcal/mol·Å². Density and pressure were equilibrated for 200 and 600 ps, respectively, at 310 K under an NTP ensemble, whereas heavy atoms were still constrained. Triplicate MD simulations of 1 μs and 100 ns (ns) long for p53 and p53−EGCG complexes were run with the pmend.cuda module in Amber22. A time step of 2 fs were considered for MD simulations, removing any constraints, and under an *NPT* ensemble. Long-range electrostatic interactions were treated using the particle mesh Ewald (PME) algorithm,[53] and short-range electrostatic and van der Waals and interactions were set to 10 Å. The bond length between the hydrogen atoms and the linked heavy atom was constrained using the SHAKE algorithm.[54] A single trajectory was generated for each system by concatenating triplicate MD simulations: 1 μs for p53, 100 ns for p53-ligand, and a single 500 ns MD simulation for p53's R2−1 and R1−3. From the trajectory coordinates, the root-mean-square deviation (rmsd), radius of gyration (R_g), clustering analysis, and principal component analysis were analyzed. Images were made with PyMOL.[55]

2.3. Binding Free-Energy Studies with mmgbsa and mmpbsa.
The MMGBSA and MMPBSA methods present in the MMPBSA.py of AMBER simulation software[56] were chosen to evaluate the binding free energy (ΔG). The ΔG values were determined during the equilibrated simulation time from the single concatenated MD trajectories considering an ionic strength of 0.15 M and implicit solvent models.[57] As mentioned elsewhere, the ΔG values and per-residue decomposition energies using these methods were determined.[58]

2.4. Molecular Docking.
For molecular docking, we employed nine different conformations of the NTD of p53. These nine conformations were obtained by selecting the top 3 most populated clusters from the initial 3 μs MD simulations (see Section 2.2). However, ECGC structures were obtained from PubChem (CID: 65064)[59] and prepared using Avogadro.[60] Two rounds of molecular docking were performed by using four software products: MOE (MOE, 2016), AutoDock Vina,[62] AutoDock4,[63] and SwissDock.[64] P53 structures were prepared with MOE for the MOE docking, whereas AutoDock Tools[63] for AutoDock Vina and AutoDock4. The initial round of molecular docking was conducted with a blind approach, allowing us to explore potential binding pockets that the software could detect within the various p53 conformations. In the subsequent round, we specifically targeted the region from Trp23 to Lys24 and from Pro47 to Thr55, which are known to be involved in ECGC binding, as reported by ref 40. Consequently, the grid boxes in all four software applications were configured to encompass these specific residues.

2.5. Structural and Interaction Analyses.
A structural comparison between systems was performed using Chimera software.[65] Furthermore, interaction analysis was conducted using Molecular Operating Environment.[61] Moreover, an evaluation of p53 residue interactions was carried out using the Residue Interaction Network Generator web service,[66] with the following parameters: nodes set at "closest", edges set to "all", and distance thresholds set to "strict". Additionally, the network was constructed using Cytoscape, employing a circular layout based on chains, where Chain-B represented EGCG.[67]
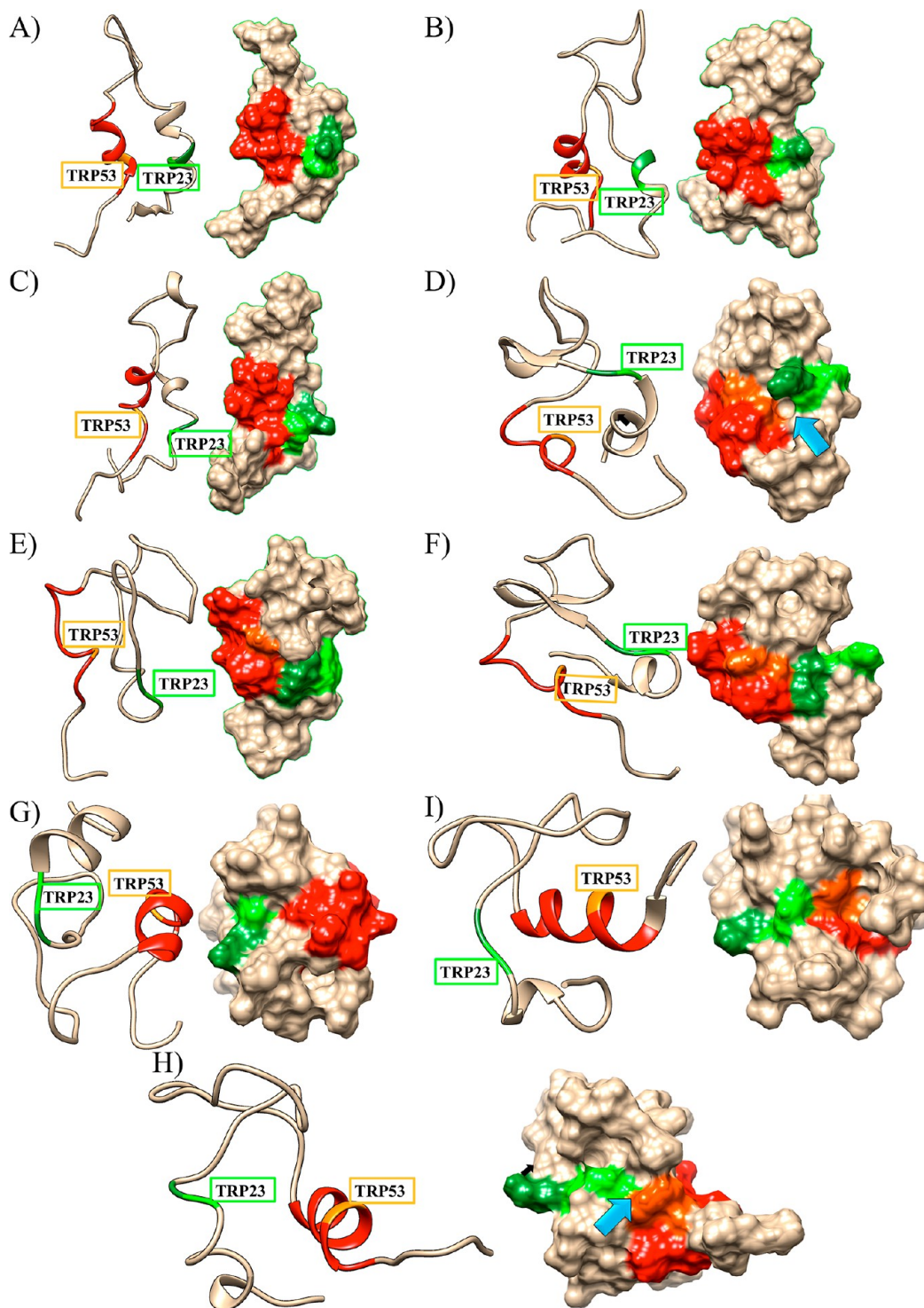
Figure 1. 3D structure visualization with ribbon (left) and its surface (right) of: (A) R1−1, (B) R1−2, (C) R1−3, (D) R2−1, (E) R2−2, (F) R2−3, (G) R3−1, (H) R3−2, and (I) R3−3. Color code: Trp23−Lys24 is colored green, and Pro47−Thr55 is red. Trp23 is highlighted in light green, and Trp53 is shown in orange-red. The blue arrow points to the region where Trp23 and Trp53 surfaces are in touch.

3. RESULTS AND DISCUSSION

3.1. Molecular Dynamics of p53. Due to the intrinsic disorder of the NTD region, we conducted triplicate microsecond MD simulations to obtain a p53 NTD structure closely resembling a conformation susceptible to EGCG binding, or one potentially induced by EGCG. These three MD simulations exhibited distinct behaviors throughout the microsecond duration, as indicated by root-mean-square deviation (rmsd)

and radius of gyration (R_g) analyses (see Figure S1). While Runs 1 (R1) and 3 (R3) displayed intermittent periods of stability, neither run maintained sustained stability, which was expected due to NTD́ known disorder. Conversely, the second run (R2) demonstrated notable stability from 300 to 1000 ns (Figure S1), with a slight deviation around 700 ns before reaching convergence. Consequently, the three most populated con-

Table 1. Interactions between ECGC and p53′s Residues Observed in the Blind Docking[a]

	R1-1	R1-2	R1-3	R2-1	R2-2	R2-3	R3-1	R3-2	R3-3
Pro13		A	A&M						A&M
Leu14			M	V			A&V		A,M,S,V
Ser15			V				V		A&M
Gln16						S&V	V	M	A
Glu17									
Thr18							A		
Phe19	A	S				S&V			
Ser20			V	M				M	
Asp21				M					
Leu22	A			M			A	A	
Trp23			V	M&S	A,S,V	S&V	A	A	M,S,V
Lys24		M		A,M,S	A,M,S,V	A&V	A	A&M	
Leu25		M&S		A	A,M,S,V	A&M	A	A&M	
Leu26	A	S		A&S	A,M,S,V	A,M,S	M&S	M	
Pro27				A	A&M	A&M	M&S	A	
Glu28		M	S	A	A,M,S,V	A&M	S	A	
Asn29		M	S			A&M	M&S	V	
Asn30	A	M&V	S			A	M&S	A&V	
Val31	A	M	S	V	A,M,V		M&S	A,S,V	
Leu32	M,S,V	M	S		A,M,V			S&V	
Ser33	M&S	M	S	A	A,M,S,V			A	A
Pro34	M,S,V			A&S	A,S,V			A	A,M,S,V
Leu35	M,S,V	M		A&S	A,M,S,V	A		A	A&S
Pro36	M,S,V			A	A,M,S,V	A	A	A	S&V
Ser37	M,S,V			A	A,M,S,V	A			
Gln38	M,S,V	M			A,M,V			M	
Ala39					A&M			M	
Met40	M,S,V							M	
Asp41								M	
Asp42	A			V					
Leu43	A&V		S	V				M	
Met44	A,M,V			V					
Leu45	A&M	V		V				V	
Ser46	V			V					
Pro47	S&V		A&M						
Asp48									
Asp49		V		V				V	
Ile50	A		A					V	
Glu51		A	A&M				V		
Gln52		A,S,V		M			V	S&V	
Trp53	A	A,S,V		M		A	M&V	A,S,V	A,M,S,V
Phe54			A,M,V	M		A	M,S,V	S	A,M,S,V
Thr55		A&S	V				M,S,V		
Glu56		A&S	A,M,V				M&S	S&V	
Asp57		A&S	A&S				M&S		A,M,S,V
Pro58		A,S,V	M				S		A,M,S,V
Gly59		A,S,V	A&M						A,M,S,V
Pro60		A							A,M,S,V
Asp61		A		M					A,M,S,V

[a]Abbreviation: A: AutoDock, M: MOE, S: Swissdock, and V:AutoVina. Color code: Yellow: interaction found within 2 software, orange: 2 software, blue: 3 software, and green: all 4 software.

formations from each MD simulation were selected to evaluate EGCG binding, as illustrated in Figure 1.

The p53 NTD regions of Trp23−Lys24 and Pro47−Thr55 are involved in EGCG binding,[40] and these regions are colored in green and red, respectively, in Figure 1. On the other hand, given that Trp23 and Trp53 exhibit the most significant chemical shift changes upon EGCG binding,[40] these residues were highlighted using light green and red-orange, respectively.

Interestingly, in all conformers, these two regions were significantly close. However, Trp23 and Trp53 were not. In addition, in most cases, these regions formed an α-helical, a finding that is congruent with previous studies.[40] Moreover, these α-helices are necessary for binding proteins, such as MDM2 and MDMX on Trp23 or high mobility group box 1 proteins (HMGB1) on Trp53.[68−71]

Table 2. Interactions between ECGC and p53′s Residues Observed in the Directed Docking[a]

	R1-1	R1-2	R1-3	R2-1	R2-2	R2-3	R3-1	R3-2	R3-3
Pro13			S				A	S	A,S,V
Leu14						A	A&M	S	A,M,S,V
Ser15	M					A		S	
Gln16	M				A	A&M		S	
Glu17						A		S	
Thr18	V		V			A	A&M		
Phe19	V	A&S	S&V			A&M		S	
Ser20			M	A	S	S			
Asp21	V		M		S				
Leu22	V		M&V			M,S,V	A&M	A,M,V	
Trp23			A&M	A&S	A,S,V	M,S,V	A&M	A,M,V	A,M,S,V
Lys24			A&M	A,M,S	A,S,V	M,S,V	A&M	M&V	
Leu25		A	M	A	A&V	A		M&V	
Leu26	V	A,M,S	V	M&V	A&V	M,S,V	S	S	
Pro27			A	V	A&M		S&V	A,M,V	
Glu28		S	A	V	A		S&V	A	
Asn29	S		V				S&V		
Asn30	A,S,V	M&V	S&V				S&V	A&M	
Val31	A		S		A		A,S,V	A,M,V	
Leu32					A	A	A	A,M,V	
Ser33					A		A&M	A,M,V	A
Pro34				S	A&V	A,M,V	A&M	M	A,M,S,V
Leu35				S	A&V	M&V	A	A&M	A,M,S
Pro36				S	A&V	M&V	A&M	A,M,V	A,M,S
Ser37					A		V		
Gln38									
Ala39									
Met40				S		A			
Asp41	S								
Asp42	A&S								
Leu43	A&S					A			
Met44	A&S					A			
Leu45	A&S	M&V	A			A			
Ser46			A						
Pro47			A	V	M			S	
Asp48					M			S	
Asp49	A&M	A,M,V	S		M				
Ile50	S,V		A		M	A			
Glu51			A&S		M			S	
Gln52	A&M	A,M,V	S	A					
Trp53	A,M,S,V	A,M,V	S&V	A,M,V	M	V		A&V	A,M,S,V
Phe54		A	A&M	A&M	M&S	S	S&V		A,M,S,V
Thr55	M	A&S	M	A	S	S	S&V		
Glu56	M	A&S	A	A	S	S	S&V		
Asp57	M	S		A			S&V		A,M,S,V
Pro58		A,M,V					S&V		A,M,S,V
Gly59		M&V							
Pro60									M&S
Asp61				A					A,M,S,V

[a]Abbreviation: A: AutoDock, M: MOE, S: Swissdock, and V: AutoVina. Color code: yellow: interaction found within 2 software, orange: 2 software, blue: 3 software, and green: all 4 software.

In the conformation that represents the most populated state observed in the first run (R1−1), both regions formed an α-helical structure (Figure 1A). Trp23 and Trp53 were oriented toward opposite sides of the p53 NTD; however, it is worth noting that the Trp23 surface is in contact with the Pro47−Thr55 region (Figure 1A). R1−2 and R1−3 also displayed almost identical characteristics within the regions of interest (Figure 1B,C). The main difference from R1−1 is that within

Trp23−Lys24, R1−2 and R1−3 lost their α-helical conformations.

In R2−1, Trp23 and Trp53 were close and faced the same side of the p53 NTD. Moreover, there was an opening between Trp23 and Trp53 (as shown by the blue arrow in Figure 1D). This outcome is fascinating because this opening is the only one seen between Trp23−Lys24 and Pro47−Thr55, suggesting a specific binding pocket for the union of EGCG. In addition,
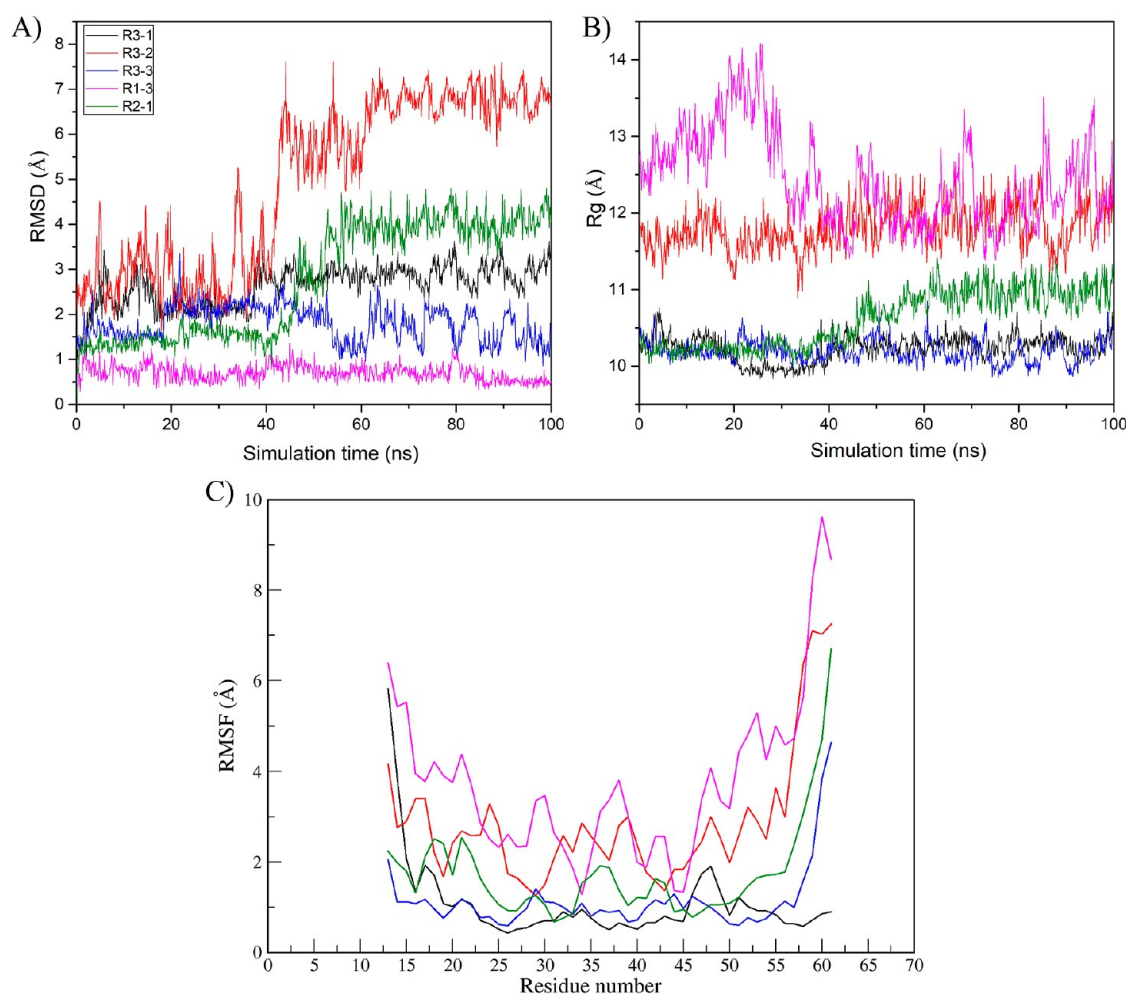
Figure 2. Trajectory analysis of R1−3, R2−1, R3−1, R3−2, and R3−3 systems through: (A) rmsd, (B) R_g, and (C) RMSF. Color code: R1−3 (pink), R2−1 (green), R3−1 (black), R3−2 (red), and R3−3 (blue).

none of the regions of interest possessed a specific 3D structure. On the other hand, R2−2 and R2−3 had similar characteristics to R2−1; however, there was a key difference: they were farther away and did not have an opening between the regions (Figure 1E,F). As this run achieved a state of convergence, it is noteworthy that none of these three structures had any α-helix around Trp53. Similarly, for Trp23, an α-helix was absent in two of the three structures, while in the most populated structure, Trp23 was positioned outside the α-helix (Figure 1D−F), which goes according to the unfolded nature of NTD.[72]

Finally, R3−1, R3−2, and R3−3 possessed similar characteristics within the region of interest (Figure 1G−I), namely, Pro47−Thr55 formed an α-helical structure, while Trp23−Lys24 did not form a specific 3D structure. Additionally, the surface between these regions was highly lumpy. Although these regions did not possess a clear opening as did R2−1, this uneven surface might have facilitated EGCG binding. In addition, R2−1 and R3−2 were the only conformations with Trp23 and Trp53 surfaces bonded together (as shown by the blue arrow in Figure 1). Therefore, R2−1 and the conformation of the third run (R3) might have generated the most favorable interactions of EGCG and the regions Trp23−Lys24/Pro47−Thr55.

3.2. Molecular Docking. Blind docking was carried out using four different software programs to determine whether some NTD p53 conformations enhanced the union of EGCG with regions of interest. The interaction between EGCG and

p53 residues is detailed in Table 1, while affinity values are presented in Table S1.

EGCG could not reach the region of interest in most of these conformations. The only partial exception to this condition was observed in the AutoDock-generated docking results for R2−3 and R3−2. Both residues had interactions with Trp23, Lys24, and Trp53, whereas R2−3 additionally exhibited interactions with Phe54. Furthermore, as seen in the column interactions detected by ≥2 software tools, most of these conformations significantly enhanced EGCG binding, primarily within the 20−30 s or 50 s range of residues. Specifically, in the 20−30 s range, we observed R2−1, R2−2, R2−3, and R3−2, while in the 50 s range, interactions with R1−2, R1−3, R3−1, and R3−3 were notable. Moreover, R1−1 exhibited a promising EGCG binding site around residues 30−40 s.

Since blind docking did not provide sufficient insights into whether some conformations enhanced EGCG binding to a desired region, we performed molecular docking directed toward Trp23−Lys24 and Pro47−Thr55. The interactions between EGCG and p53 residues are shown in Table 2, while the corresponding affinity values can be found in Table S2.

Once again, some conformations enhanced the binding of EGCG to the 20−30 s range, such as R2−2 and R2−3, or the 50 s range, exemplified by R1−1 and R1−2. On the other hand, R1−3, R2−1, R3−1, R3−2, and R3−3 were able to interact with both regions. In this conformation, some software showed

EGCG interacting with both areas simultaneously, while others showed an interaction with one region at a time (Table 2). Noticeably, this conformation exhibited both types of interactions, and features of at least three of the key residues were detected at least twice. It is worth noting that R2−2 also possesses these qualifying characteristics. However, we prioritized molecules where many key residues were detected or where Trp23−Trp53 interactions were observed at least twice. Therefore, these five conformations were selected to further test their affinity toward EGCG during MD simulations. In this selection process, their affinity values were not considered as we prioritized the locations of these conformations. In addition, docking results often exhibit a less-than-ideal level of accuracy.[73]

3.3. Conformational Stability of p53−EGCG Systems.

R1−3, R2−1, R3−1, R3−2, and R3−3 systems initiated triplicate MD simulations lasting 100 ns each. EGCG remained bonded to p53 in all of the systems, which is notable because some of these complexes did not reveal a particularly high binding affinity during the docking analysis. Thus, EGCG, to some extent, can have stable interactions with the Trp23−Lys24 and Pro47−Thr55 regions. To conduct an in-depth analysis and comparison of system stability and behavior, we analyzed their trajectories using rmsd, R_g, and root-mean-square fluctuation (RMSF) (Figure 2). rmsd is a metric that calculates the mean distance between the atoms of two structures,[74] enabling an assessment of the alterations that systems experience from the reference structure throughout the 100 ns simulation.

As can be seen in Figure 2A, the R3−2 (red) system fluctuated and changed the most during the 100 ns period. Due to the high level of fluctuation at the beginning, the changes that R3−2 experienced might be related to poor stability between EGCG and p53 in the reference structure. However, as the simulation continued, EGCG could have induced a conformation change that allowed the system to stabilize from 60 to 100 ns. This change could also be due to the movement of EGCG within the p53 structure, but as shown in the RMSF analysis, p53 residues experienced a significant change (Figure 2C; red). Therefore, it is likely that EGCG generated a conformational change in the R3−2 structure. A similar change was also observed to a lesser extent with R3−1 and R2−1. Moreover, R2−1 experienced a conformational change between 40 and 50 ns and stabilized at 50−100 ns (Figure 2A; green). On the other hand, R3−1 experienced a minor conformational change at approximately 40 ns and stabilized at 40−100 ns (Figure 2A; black). However, the change in R3−1 might not be related to p53 because the residues of R3−1 did not experience a significant change in RMSF (Figure 2C; black), potentially indicating that the change could be due to a shift in the EGCG location.

R3−3 and R1−3 did not experience a significant change during the 100 ns period. Nevertheless, R3−3 exhibited a remarkable constant fluctuation, which might be related to the poor stability of EGCG−p53 (Figure 2A; blue). Furthermore, R1−3 manifested remarkably high stability from the beginning, possibly due to a favorable interaction between EGCG and p53 (Figure 2A; pink).

R_g indicates a system's degree of compactness: a high R_g value corresponds to low compactness, while a low R_g value corresponds to high compactness.[75] Thus, R_g is another indicator of the conformational changes that the system experienced during the simulation. As shown in Figure 2B, the R_g of R1−3 (pink) is quite the opposite of what was seen in the rmsd analysis: the R1−3 system experienced the least compact-

ness and had constant fluctuations, particularly during the first ns of the simulation as the system experienced a peak, which might suggest a rapid conformational change. Taking these findings into account along with the stability observed in the rmsd analysis and the pronounced fluctuations noticed throughout the residues of p53 in RMSF, it is plausible to infer that EGCG establishes a remarkably stable interaction with the R1−3 region of p53, as indicated by the rmsd analysis. This interaction, in turn, induces a swift conformational transition in p53, leading to a highly stable and noncompact conformation, as R_g and RMSF suggest.

R_g shows that R3−2 has a notably low level of compactness, which is expected, as rmsd indicated that R3−2 suffers a significant conformational change. However, we did not see the same tendency in R_g as we saw in rmsd, which might indicate that some of the changes observed in rmsd could be due to the movement of EGCG. The R_g in R2−1 also revealed that the system had a stable conformation from 60 to 100 ns, as seen in rmsd analysis. This finding suggests that the movement in both graphs is due to moderate conformational change within p53 and not due to movement of EGCG. On the other hand, R3−1 and R3−3 exhibited low R_g values and high stability. This condition along with the high fluctuations and changes seen in the rmsd could indicate a constant movement of EGCG within p53.

RMSF is used to quantify the extent to which a particle deviates from its initial position; and, in this context, it was utilized to assess the changes each residue experienced throughout the simulation.[75] As mentioned earlier, p53 in the R1−3 system exhibited the most substantial alterations across numerous residues, particularly in the Trp23−Lys24 and Pro47−Thr55 regions. Similarly, the R3−2 system caused significant modifications within a majority of residues, particularly in the highlighted regions of interest (Figure 1C). Consequently, both conformations underwent notable changes in the specified p53 residues. As previously mentioned, R1−3 exhibits high stability in rmsd. Therefore, the observed change may be attributed to a rapid conformational shift induced by EGCG. On the other hand, R3−2 changes might be related to the instability of the p53 structure or to changes induced by EGCG. Due to the change seen in rmsd and the stability of R_g, this outcome might be related to the constant fluctuation of the system until the EGCG and p53 became stable around 40 ns.

R2−1 generated a moderate change within p53 residues (Figure 2C; green), demonstrating, as previously described, that EGCG induced a moderate change and had a significantly stable interaction with the R2−1 conformation.

R3−1 and R3−3 systems did not cause a significant change in the p53 structure (Figure 2C). Moreover, both systems experienced a change and caused a fluctuation in the rmsd, which might indicate poor stability of EGCG and a constant movement within p53.

In the RMSF analysis, we evaluated the change in the residues of interest: Trp23−Lys24 and Pro47−Thr55. For the Trp23−Lys24 region, systems R3−1, R3−3, R1−3, and R2−1 caused a significant decrease in deviation. This outcome suggests that EGCG had a stable interaction with this region in all of these systems, with low fluctuations or changes. This outcome was not seen in R3−2, which experienced a peak in this region. Therefore, part of the movement seen in the rmsd is due to the movement of EGCG from its initial point, which generated a conformational change within the Trp23−Lys24 region.
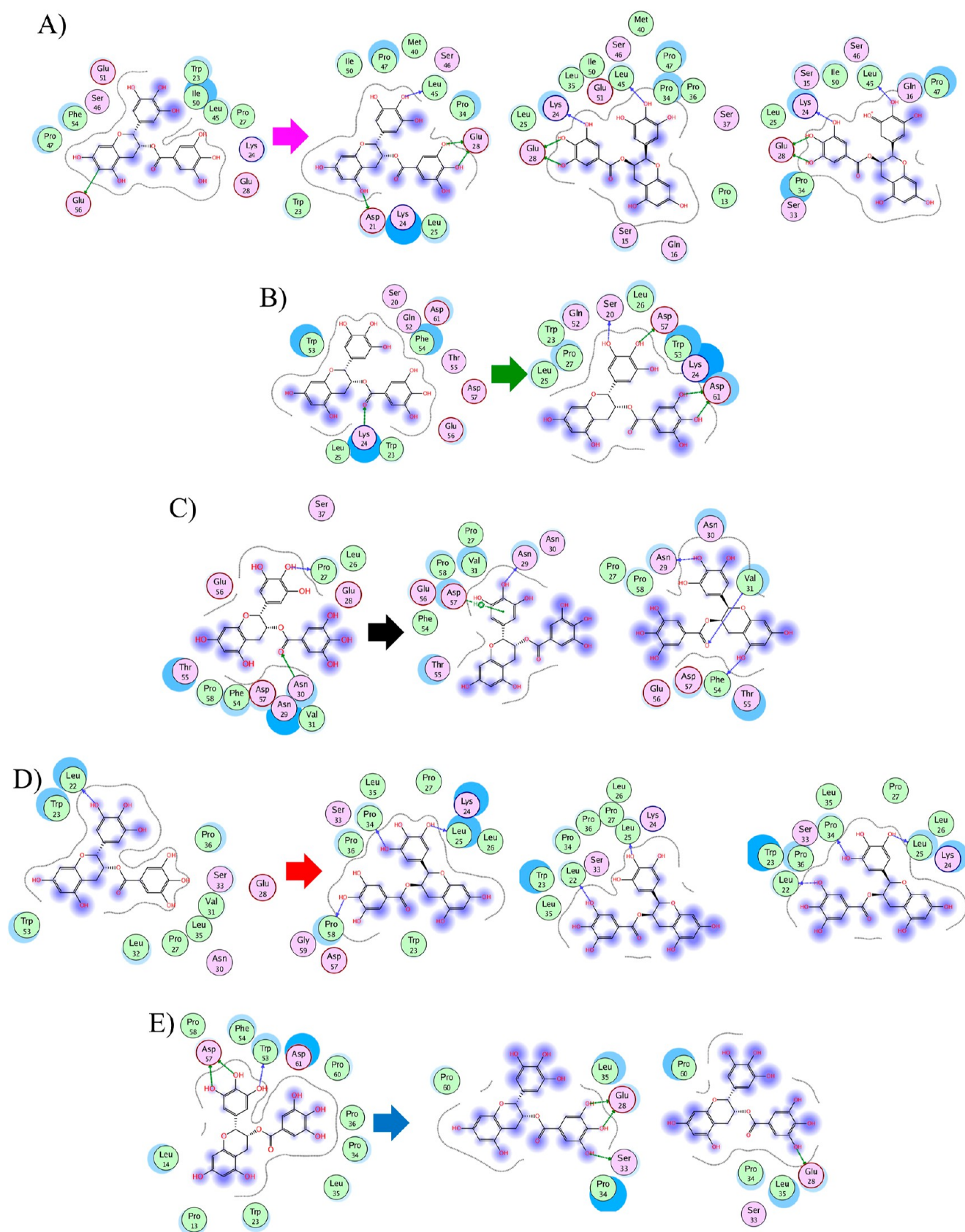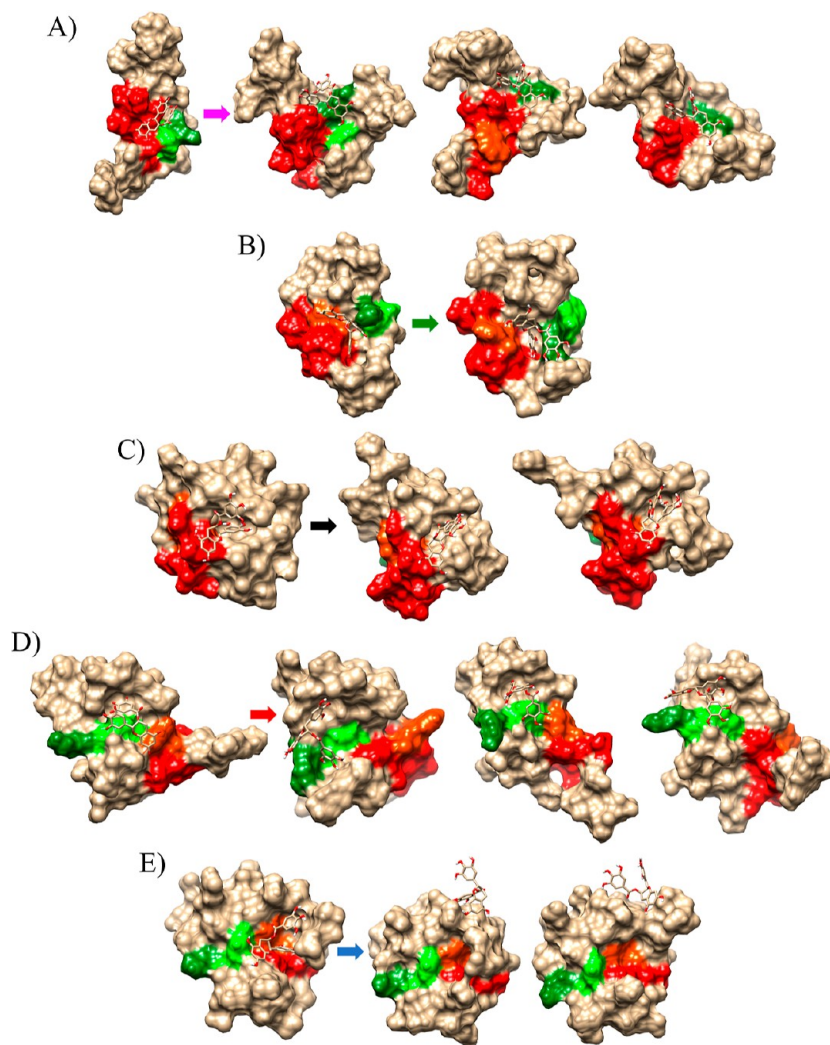
Figure 3. 2D analysis of Reference structures → significant clusters of: (A) R1−3, (B) R2−1, (C) R3−1, (D) R3−2, and (E) R3−3. Color code: Arrows: R1−3 (pink), R2−1 (green), R3−1 (black), R3−2 (red), and R3−3 (blue).

In the Pro47−Thr55 region, R3−1, R3−2, and R1−3 manifested similar behavior and had notable high peaks. This

finding suggests that EGCG might have lost interaction with this region in some systems. On the other hand, R2−1 and R3−3

Figure 4. 3D Analysis of reference structures → significant clusters of: (A) R1−3, (B) R2−1, (C) R3−1, (D) R3−2, and (E) R3−3. Color code: surface: Trp23−Lys24 is colored green, and Pro47−Thr55 is red. Trp23 is highlighted in light green, and Trp53 is shown in orange-red.

had a low change within this region accompanied by a constant increase as residues moved near the C-terminal.

To summarize the trajectory analysis, R1−3 and R2−1 systems had high stability, whereas R2−1 generated a low change in the regions of interest.

3.4. Interactions between p53 and EGCG. In this context, systems were primarily selected based on the p53 regions of interactions. We wanted to analyze each system's most significant interactions throughout the MD simulation. Therefore, we selected the interactions seen in the most significant clustering structures within each system.

In the R1−3 system, three significant conformations were detected. These structures and their interactions can be seen in Figures 3A and 4A. The reference structure of this system generated interactions with Trp23, Lys24, Pro27, Glu28, Leu45, Ser46, Pro47, Ile50, Glu51, Phe54, and Glu56 (Figure 3A).

In the MD simulations, the most populated cluster generated interactions with Asp21, Trp23, Lys24, Leu25, Glu28, Pro34, Met40, Leu45, Ser46, Pro47, and Ile50. The second-most populated cluster had interactions with Pro13, Ser15, Gln16, Lys24, Leu25, Glu28, Pro34, Pro36, Ser37, Met40, Leu45, Ser46, Pro47, Ile50, and Glu51. Furthermore, the third-most populated cluster had interactions with Ser15, Gln16, Lys24, Leu25, Glu28, Ser33, Pro34, Leu45, Ser46, Pro47, and Ile50.

The residues that maintained interactions with EGCG throughout the simulation were Lys24, Glu28, Leu45, Ser46, Pro47, Ile50, and Glu51 (Figure 3A). This system had significant interactions with four residues that are key in the interaction of EGCG and p53.[40]

There were some interesting structural changes that p53 suffered. First, the most populated structure closely resembles the reference structure. Moreover, in the second and third-most populated structures, Trp23 changed its location to another face of the p53 structure (Figure 4A). Trp53 also changed its location to face EGCG. Nevertheless, both residues did not face the same direction in either of these three structures.

In the R2−1 system, there was only one significant structure cluster, which is encouraging due to the potential binding pocket seen in Figure 1D. At the reference structure, EGCG had interactions with Ser20, Trp23, Lys24, Leu25, Gln52, Trp53, Phe54, Thr55, Glu56, Asp57, and Asp61. In the most populated structure, EGCG had interactions with Ser20, Trp23, Lys24, Leu25, Leu26, Pro27, Gln52, Trp53, Asp57, and Asp61 (Figure 3B). Thus, EGCG had significant interactions with four of the residues of interest; and, importantly, two of these interactions were with Trp23 and Trp53, the most relevant residues in EGCG binding.[40] The structural change during the MD simulation revealed a further increase in the possible binding

Table 3. Binding Free-Energy Components of p53−EGCG Complexes Calculated Using the MMGBSA Approach (Values kcal/mol)

system	ΔE_{vdw}	ΔE_{ele}	$\Delta G_{ele,sol}$	$\Delta G_{npol,sol}$	ΔG_{bind}
Run3−1	−26.69 ± 2.0	−18.15 ± 4.7	34.63 ± 12.0	−3.03 ± 0.15	−13.24 ± 2.0
Run3−2	−26.94 ± 4.0	−25.39 ± 10.0	42.13 ± 11.0	−3.38 ± 0.50	−13.59 ± 3.0
Run3−3	−20.5 ± 4.0	−44.27 ± 13.0	58.83 ± 18.0	−3.37 ± 0.40	−9.75 ± 3.0
Run1−3	−23.86 ± 4.0	−73.93 ± 13.0	84.63 ± 11.0	−4.40 ± 0.4	−17.58 ± 3.0
Run2−1	−26.57 ± 5.0	−57.34 ± 19.0	73.11 ± 18.0	−4.22 ± 0.50	−15.43 ± 3.0

pocket within Trp23 and Trp53 (Figure 4B). Moreover, there was a significant movement in the Trp23−Lys24 region. Lys24 moved toward the surface of p53, which allowed the direct interaction of Trp23 with EGCG. This movement further enhanced the penetration of EGCG into p53 NTD during the MD simulation. The placement of EGCG at this position may explain the presence of only one significant cluster in the MD simulation given that this p53 conformation would be able to maintain a stable core and a highly compact structure.

In R3−1, there were two significant clusters, and the most populated cluster interacted with Pro27, Asn29, Asn30, Val31, Phe54, Thr55, Glu56, Asp57, and Pro58. The second-most populated cluster interacted with Pro27, Asn29, Asn30, Val31, Phe54, Thr55, Glu56, Asp57, and Pro58 (Figure 3C). Consequently, the same residues were seen in both clusters. The reference structure had interactions with Leu26, Pro27, Glu28, Asn29, Asn30, Val31, Phe54, Thr55, Glu56, Asp57, and Pro58. EGCG interacted with residues around 20 s and W-23 and K-24 in other structures during the second docking analysis. However, EGCG did not interact with the Trp23−Lys24 region and interacted with only two residues in the Pro47−Thr55 region. The structural changes in this model indicate that EGCG enhanced the binding pocket within the core of p53 (Figure 4C).

In the R3−2 system, the reference structure exhibited interactions with Leu22, Trp23, Pro27, Glu28, Asn30, Val31, Leu32, Ser33, Leu35, Pro36, and Trp53 (Figure 3D). Simultaneously, it is remarkable that Trp23 and Trp53 were proximal, suggesting an enhanced interaction of EGCG with these key residues. However, in all three significant cluster structures, EGCG did not interact with Trp53 (Figure 3D) due to the movement of EGCG toward Lys24, as indicated in the structural changes (Figure 4D). Therefore, as hypothesized in the trajectory analysis, the high movement of this system in the rmsd analysis is due to EGCG movement. The most populated cluster interacted with Trp23, Lys24, Leu25, Leu26, Pro27, Ser33, Pro34, Leu35, Pro36, Asp57, Pro58, and Gly59. The second-most populated cluster interacted with Leu22, Trp23, Lys24, Leu25, Leu26, Pro27, Ser33, Pro34, Leu35, and Pro36. The third-most populated cluster interacted with Leu22, Trp23, Lys24, Leu25, Leu26, Pro27, Ser33, Pro34, Leu35, and Pro36. Thus, in this system, p53 had significant interactions with Trp23, Lys24, Leu25, Leu26, Pro27, Ser33, Pro34, Leu35, and Pro36.

Finally, in the R3−3 system, the reference structure interacted with Pro13, Leu14, Trp23, Pro34, Leu35, Pro36, Trp53, Phe54, Asp57, Pro58, Pro60, and Asp61. However, the two significant clusters lost all interactions with the Trp23−Lys24 and Pro47−Thr55 regions. The most populated clusters interacted with Glu28, Ser33, Pro34, Leu35, and Pro60. The second-most populated cluster interacted with Glu28, Pro34, Leu35, and Pro60 (Figure 3E). Hence, despite the initial placement of EGCG within a region of p53 flanked by Trp23 and Trp53, it eventually migrated away from this vicinity (Figure 4E).

Therefore, R2−1 and R1−3 were the only systems that allowed EGCG to interact with both regions of interest. However, R2−1 was the only system in which EGCG interacted with Trp23 and Trp53. On the other hand, R3−1 had stable interactions with the Pro47−Thr55 region, while R3−2 had a stable interaction with Trp23−Lys24.

3.5. MMGBSA Calculations. MMGBSA was used to estimate the strength of the interaction between EGCG and p53 within different systems. Interestingly, in line with the trajectory analysis, Run1−3 (−17.58 kcal/mol) and Run2−1 (−15.43 kcal/mol) were the two systems in which EGCG exhibited the most robust interactions with the NTD of p53 (Table 4). Notably, EGCG had interactions with both regions of interest in these two systems. R3−1 (−13.24 kcal/mol) and R3−2 (−13.59 kcal/mol) had significant interactions with only one of these regions and displayed a slightly reduced affinity toward p53 (Table 3).

In contrast, R3−3 exhibited a diminished affinity at −9.75 kcal/mol, as anticipated, due to the observed movement outside the intended binding pocket throughout the simulation (Figure 4). EGCG had interactions of similar intensities with Trp23−Lys24 and Pro47−Thr55. However, when EGCG interacted with both regions, the intensity of the interaction was slightly stronger. Additionally, it was surprising that R2−1 did not possess the highest binding strength given its pronounced induction of a binding pocket within Trp23 and Trp53 (see Figure 4). This diminished strength might be due to the same reason why a binding pocket was formed toward the core; namely, there was a reduced number of residues that can interact with EGCG (Figures 3 and 4).

A per-residue energy decomposition was conducted to elucidate the contributions of p53 residues to the MMGBSA value. These values can be seen in Table 4. As expected, the R1−3 system, involving 17 residues, generated the highest number of significant interactions throughout the MD simulation.

The nine residues with a contribution above −1 kcal/mol were Lys24, Glu28, Pro34, Leu35, Pro36, Leu45, Ser46, Pro47, and Ile50. Three of the desired residues had an affinity higher than −1 kcal/mol. R3−1 and R3−2 followed suit, with 11 interactions each and 6 interactions above −1 kcal/mol. In R3−1, the residues present were Asn29, Asn30, Val31, Thr55, Asp57, and Pro58. R3−1 interacted with only one of the desired residues. On the other hand, for R3−2, residues Trp23, Lys24, Leu25, Pro27, Leu35, and Pro36 generated interactions with the whole Trp23−Lys24 region.

The four systems with the highest interactions within Table 4 were with R2−1. Thus, even though R2−1 had interactions with 10 fewer residues than did R1−3, R2−1 generated a highly closed MMGBSA value. Consequently, the interactions that EGCG can generate in the induced binding pocket have a significant strength. The residues that generated a higher value than −1 kcal/mol in R2−1 were Trp23, Lys24, Leu25, and Trp53. Therefore, in the R2−1 system, EGCG interacted with

Table 4. Per-Residue Energy Decomposition for p53-Ligand Complexes after 100 ns Long MD Simulations (kcal/mol)

residue	RUN3−1	RUN3−2	RUN3−3	RUN1−3	RUN2−1
Ser15				−0.19	
Gln16				−0.606	
Ser20					−0.509
Leu22		−0.777			
Trp23		−2.217		−0.894	−1.427
Lys24		−1.7975		−1.56	−3.9465
Leu25		−3.445		−0.433	−1.09
Leu26	−0.945	−0.754			−0.9025
Pro27	−0.617	−1.0965		−0.519	−0.849
Glu28	−0.329		−2.0355	−3.515	
Asn29	−1.649				
Asn30	−1.043		−0.413		
Val31	−1.424				
Leu32					−0.4335
Ser33			−1.029	−0.44567	
Pro34		−0.658	−1.908	−2.32733	
Leu35		−1.1325	−1.7513	−1.358	
Pro36		−1.919		−1.281	
Met40				−0.295	
Met44				−0.18967	
Leu45				−1.85233	
Ser46				−1.01467	
Pro47				−1.47767	
Ile50				−1.888	
Gln52					−0.702
Trp53		−0.380			−2.4655
Phe54	−0.320				
Thr55	−1.496				
Glu56	−0.753				
Asp57	−1.253				
Pro58	−1.072	−0.359			
Gly59			−0.3555		
Pro60			−0.7495		

Trp23, Lys24, and Trp53, generating significantly high energetic interactions.

3.6. Structural Analysis of p53−EGCG Conformation.

As previously mentioned, Trp23−Lys24 and Pro47−Thr55 were selected as regions of interest based on the study by Zhao et al.,[40] which was based on chemical shift perturbations detected by 2D NMR. Therefore, there is no way to determine whether this shift is due to direct interaction with EGCG or a conformational change provoked by it.[76] Consequently, to further assess the possibility of a conformational change, we analyzed the interactions induced by EGCG among the residues. This analysis was carried out using the Residue Interaction Network Generator web service.[66]

To effectively compare the conformational changes triggered by EGCG, we opted to contrast the interactions before the MD simulation with those within the most populated structure of each system. Notably, the initial structures were obtained from a prior MD simulation of each system, ensuring that the interactions were based on the equilibrium conditions. Additionally, system R3−3 was excluded due to the low binding affinity between EGCG and p53 (Table 3). These interactions can be seen in Figure 5.

In the R3−1 system within Trp23−Lys24, before the MD simulation, both residues had an interatomic contact (IAC) with EGCG, while Trp23 had a van der Waals interaction with Pro27

(Figure 5A; left). However, in the most populated structure, following the MD simulation, both residues retained their IAC interactions with EGCG.

Notably, Trp23 lost contact with Pro27 but formed several new van der Waals interactions and an $\pi-\pi$ stack interaction with Phe54. Additionally, Lys24 established an ionic interaction with Asp21 (Figure 5A; right).

Moving to the Pro47−Thr55 region, Pro47 and Glu51 displayed IAC interactions with EGCG before the MD simulation and formed a hydrogen bond between them. Regrettably, these interactions were lost during the simulation, and Glu51 dissociated from the EGCG network (Figure 5A). Moreover, Trp53 and Phe54 were both involved in interactions with Ile50, and Trp53 interacted with Phe19, Leu26, Pro27, and Asn30. Following the MD simulation, Ile50 maintained its interaction with Trp53 and Phe54. Trp53 retained only the interaction with Asn30 while establishing a new one with Asp49. However, as mentioned above, Phe54 generated interactions with Trp23. Finally, after the MD simulation, Thr55 went out of the EGCG network, while Gln52 changed its interaction with Pro13 to form a hydrogen bond with Asp49. Therefore, although most of the residues of interest remained part of the EGCG network, several key alterations were observed. For instance, two residues (Glu51 and Thr55) lost all of their interactions, and some residues experienced reduced interactions. Moreover, EGCG induced a robust interaction between Phe54 and Trp23 during the simulation.

In the R2−1 system, Trp23 and Lys24 interacted with EGCG, while Trp23 had an $\pi-\pi$ stack interaction with Phe19 (Figure 5B; left). After the simulation, Lys24 generated a hydrogen bond with Pro60, and Trp23 generated a hydrogen bond with Leu25, augmenting its interactions with Phe19 (Figure 5B; right). From the other region, Glu51 formed hydrogen bonds with Phe54 and Thr55 before and after the simulation (Figure 5B). A similar pattern was observed with Trp53, which initially had multiple interactions with Pro47 and Ile50 before the simulation. Notably, Trp53 maintained interactions after the simulation, although these interactions were reduced. Gln52 established van der Waals interactions with Ser20 and Asp57 during the simulation. Finally, Asp49 entered the EGCG network by forming multiple interactions with Leu45 (Figure 5B; right). In this system, the pre-existence of a potential binding pocket between the surfaces of Trp23 and Trp53 (Figure 1B) is noteworthy. Thus, given that the majority of the interactions involving the residues of interest were preserved during the EGCG stimulus, with the emergence of Asp49, all residues of interest, except for Asp48, were integrated into the EGCG network. In addition, EGCG created new interactions among crucial residues, strongly implying that all the residues of interest play a pivotal role in forming the binding pocket induced by EGCG between Trp23 and Trp53 in this system, echoing the observation made by Zhao et al.[40]

In the R3−1 system, neither Trp23 nor Lys24 had interactions with EGCG before the MD simulation; however, both became part of the EGCG network due to some other interactions, as seen in Figure 5C (left). During the MD simulation, Lys24 disappeared from this network, while Trp23 was kept due to five downstream interactions, including the Phe54 interaction with EGCG (Figure 5C). This outcome was expected because EGCG does not interact with this region in this system. In the Pro47−Thr55 region, prior to the MD simulation, EGCG had direct contact with Trp53, Phe54, and Thr55 and some indirect contact with Pro47, Asp48, Asp49,
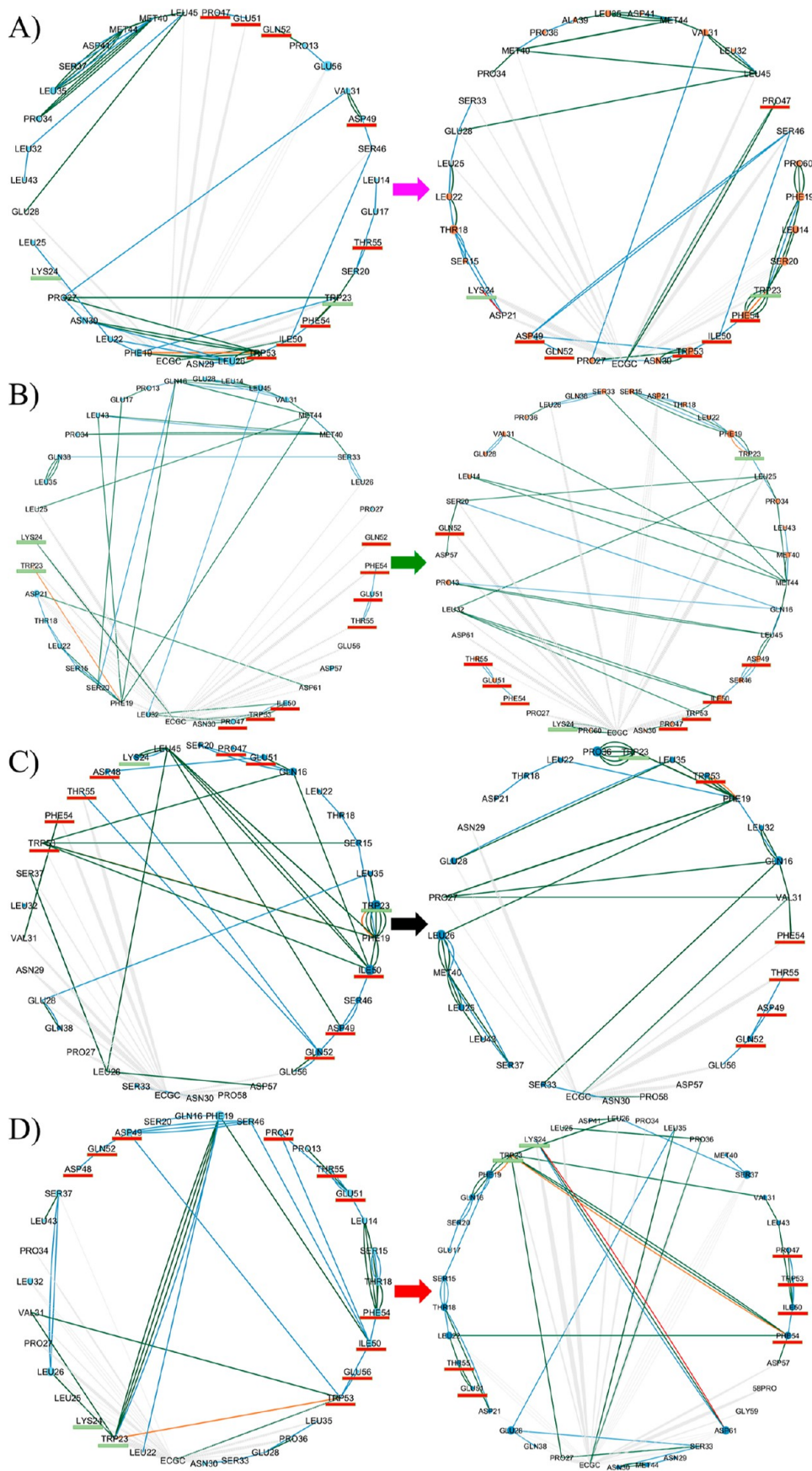
Figure 5. ECGC network analysis before MD (left) and at the most populated structure (right) of the system: (A) R1−3, (B) R2−1, (C) R3−1, and (D) R3−2. Lines color code: gray: inter-atomic contact, blue: hydrogen bond, green: van der Waals, red: ionic, and orange: π−π stack.

Ile50, Glu51, and Gln52. During the MD simulation, Pro47, Asp48, Ile50, and Glu51 left the EGCG network. Furthermore, Thr55 and Phe54 maintained a direct interaction with EGCG. Therefore, R3−1 systems do not allow EGCG to significantly influence most residues of interest.

Finally, before the MD simulation in the R3−2 system, Trp23 and Lys24 had direct contact with EGCG, and Trp23 stood out due to the interactions with Phe19 and, to a lesser extent, with Leu26, Val31, and Trp53 (Figure 5D; left). During the MD simulation, both residue-maintained interactions with EGCG. On the one hand, Trp53 maintained its interactions with Pro27, Val31, and, notably, Phe54, which stood out due to its multiple interactions (Figure 5D; right). On the other hand, Lys24 had multiple interactions with Asp61. In the other region of interest, the Trp23 residue allowed Pro47, Asp48, Asp49, Ile50, Glu51, Gln52, Trp53, Phe54, and Thr55 to become part of the EGCG network. Thus, during the MD simulation, only Pro47, Ile50, Glu51, Trp53, Phe54, and Thr55 were kept inside the EGCG network due to the interaction of Phe54 with Trp23. Therefore, the R3−2 system was shown to have a high affinity toward Trp23−Lys24 during the simulation (Figure 4D). Consequently, EGCG was only able to influence Pro47−Thr55 due to Trp53 interactions.

This comparative analysis of the influence of EGCG on various systems reveals intriguing insights into the differential impact of EGCG on specific regions. R1−3 and R2−1 systems exhibited the most substantial effect within the Trp23−Lys24 and Pro47−Thr55 regions due to their direct interactions with EGCG. On the other hand, systems R3−1 and R3−2 had high stability toward Pro47−Thr55 and Trp23−Lys24; therefore, the influence on the region was minimal. Furthermore, the R2−1 system was remarkable in that it encompassed all key residues, except for Asp48, within the EGCG network. Notably, some of these interactions were already established before the commencement of the MD simulations. This outcome strongly underscores the pivotal role of these interactions in shaping the binding pocket between Trp23 and Trp53. Moreover, the interactions of EGCG with Trp23 and Trp53 had a pronounced amplifying effect on its influence within these specific regions, as reported by Zhao et al.[40]

3.7. Extended MD Simulations for R2−1 and R3−1. As structural changes and ligand dissociation within MD simulations might not always be observed within the initial 100 ns, we chose to analyze molecules with the most favorable binding free energies, R2−1, and R1−3, through extended 500 ns MD simulations. For this purpose, we selected the most populated structure observed within the 100 ns MD simulation as it is expected to provide greater stability to each complex. Furthermore, neither complex experienced dissociation throughout the entire 500 ns simulation. Moreover, the analysis of their R_g and rmsd revealed distinct behaviors (Figure S2). On the one hand, R2−1 exhibited notable stability at the onset of the simulation, particularly evident in the R_g analysis (Figure S2). However, around 350 ns, the structure underwent a discernible structural change. Subsequently, between 400 and 500 ns, the structure found once again stability. However, it was not as stable as the first 300 ns of the simulation. On the other hand, R1−3 displayed a higher degree of instability initially, persisting until approximately 300 ns. Beyond this point, it achieved stability, albeit not as prominently as observed in the first 300 ns of R2−1 (Figure S2).

The free energy of both systems was determined using MMGBSA. The disparity between the two systems remained consistent throughout the 100 ns simulation period (Tables 3 & S3). Specifically, in the R1−3 system, ECGC exhibited a binding free energy of −15.14 ± 3.5 kcal/mol, while that of R2−1 was −12.53 ± 5.3 kcal/mol. Despite the superior affinity observed within R1−3, both systems exhibited free energy values within a comparable range. Furthermore, the per-residue decomposition of energy underscores the heightened affinity of R2−1 within the target region (Table 5). Notably, within Trp23−Lys24, the

Table 5. Per-Residue Energy Decomposition for p53-Ligand Complexes after 500 ns Long MD Simulations (kcal/mol)

residue	RUN1−3	RUN2−1
Pro19	−1.903	
Ser20		−0.799
Asp21		−0.216
Leu22		−0.807
Trp23		−1.295
Lys24	−1.607	−3.995
Leu25	−0.464	−0.838
Leu26	−0.165	−0.889
Pro27	−0.658	−0.306
Glu28	−2.830	
Leu32		−0.4335
Ser33	−0.419	
Pro34	−2.057	
Met40	−0.306	
Met44	−0.268	
Leu45	−2.555	
Ser46	−1.417	
Pro47	−2.194	
Asp49	−0.134	
Ile50	−2.642	
Gln52		−0.702
Trp53		−2.259
Phe54		−1.803
Thr55		−0.733
Glu56		−0.372

individual contributions to ECGC binding were −1.295 kcal/mol for Trp23 and −3.995 kcal/mol for K24, totaling −5.29 kcal/mol. This accounts for approximately 35% of the total binding free energy. Similarly, within Pro47−Thr55, the contributions from Gln52 (−0.702 kcal/mol), Trp53 (−2.259 kcal/mol), Phe54 (−1.803 kcal/mol), and Thr55 (−0.733 kcal/mol) sum to −5.497 kcal/mol, which constitutes approximately 37% of the total binding free energy. Therefore, 72% of the binding free energy comes from both regions, with the rest coming from nearby regions (Table 5). This analysis highlights that several residues within the desired region contribute more significantly to ECGC binding in R2−1 than that in R1−3.

To analyze the most relevant interactions within the 500 ns MD simulation, each system was used to perform cluster analysis. Within R1−3, one significant cluster was detected, whereas in R2−1, two clusters were detected. The 2 cluster goes accordingly to what was seen within the trajectory analysis (Figure S2). As can be seen in Figure 6A and Movie 1A, R1−3 completely lost its interactions with Trp23, ending up interacting with Phe19, Lys24, Leu25, Pro27, Glu28, Pro34, Met40, Leu45, Ser46, Pro47, Ile50, Glu56, Asp57, Gly59, Pro60, and Asp61. In this way, R1−3 maintained the interactions with Lys24, Leu25, Glu28, Pro34, Met40, Leu45, Ser46, Pro47, and Ile50 (Figure 6A). Therefore, this system finds stability with
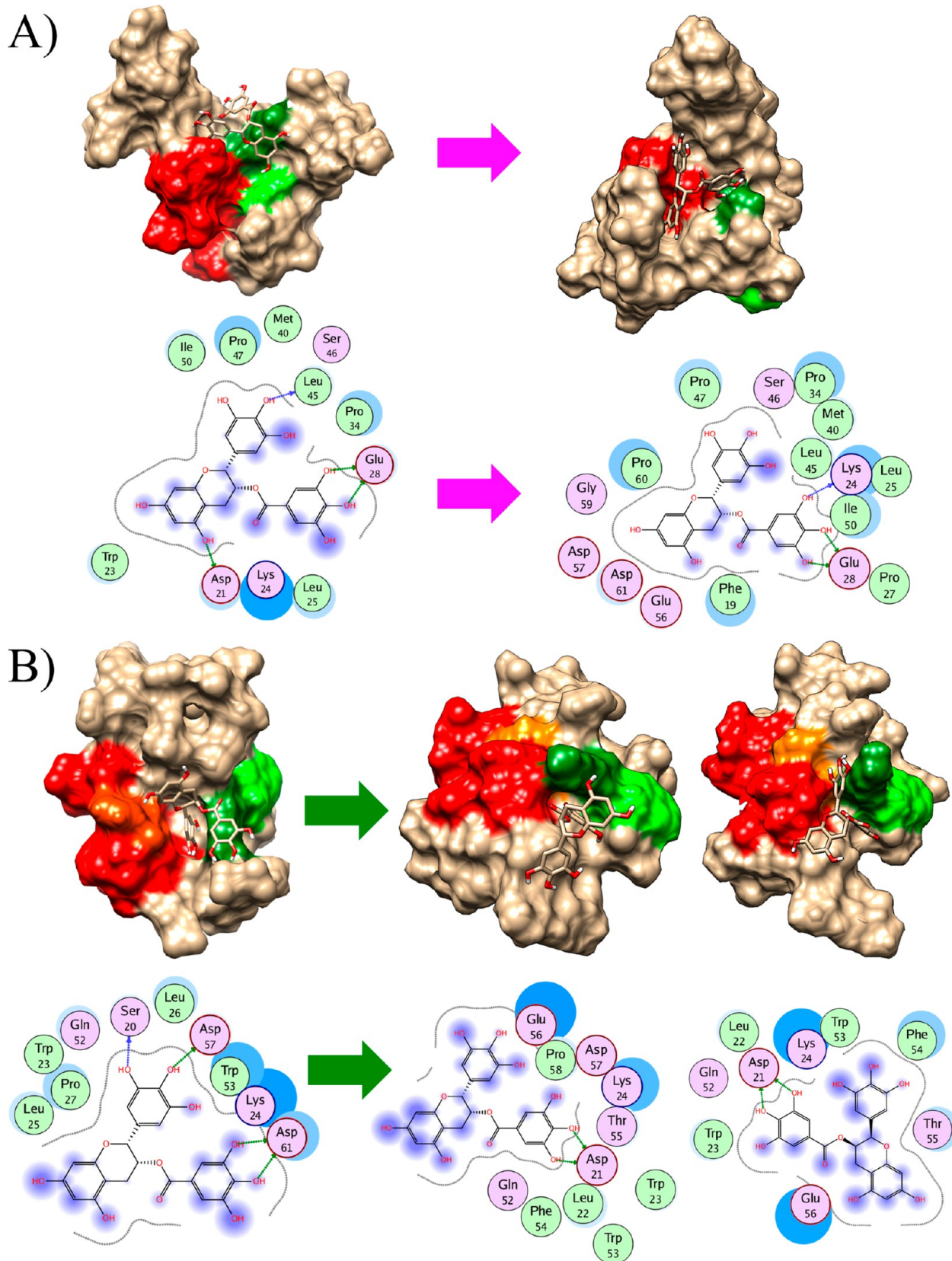
Figure 6. 3D (Up) and 2D analysis of Reference structures → Significant clusters of: (A) R1−3 and (B) R2−1. Color code: surface: Trp23−Lys24 is colored green, and Pro47−Thr55 is red. Trp23 is highlighted in light green, and Trp53 is shown in orange-red.

only three residues within the desired region: Lys24, Pro47, and Ile50 (Figure 6A). In contrast, R2−1 initially engaged in interactions with Ser20, Trp23, Lys24, Leu25, Leu26, Pro27,

Gln52, Trp53, Asp57, and Asp61 (Figure 6B and Movie 1B). Subsequently, on the most populated cluster, ECGC interacted: Asp21, Leu22, Trp23, Lys24, Gln52, Trp53, Phe54, Thr55,
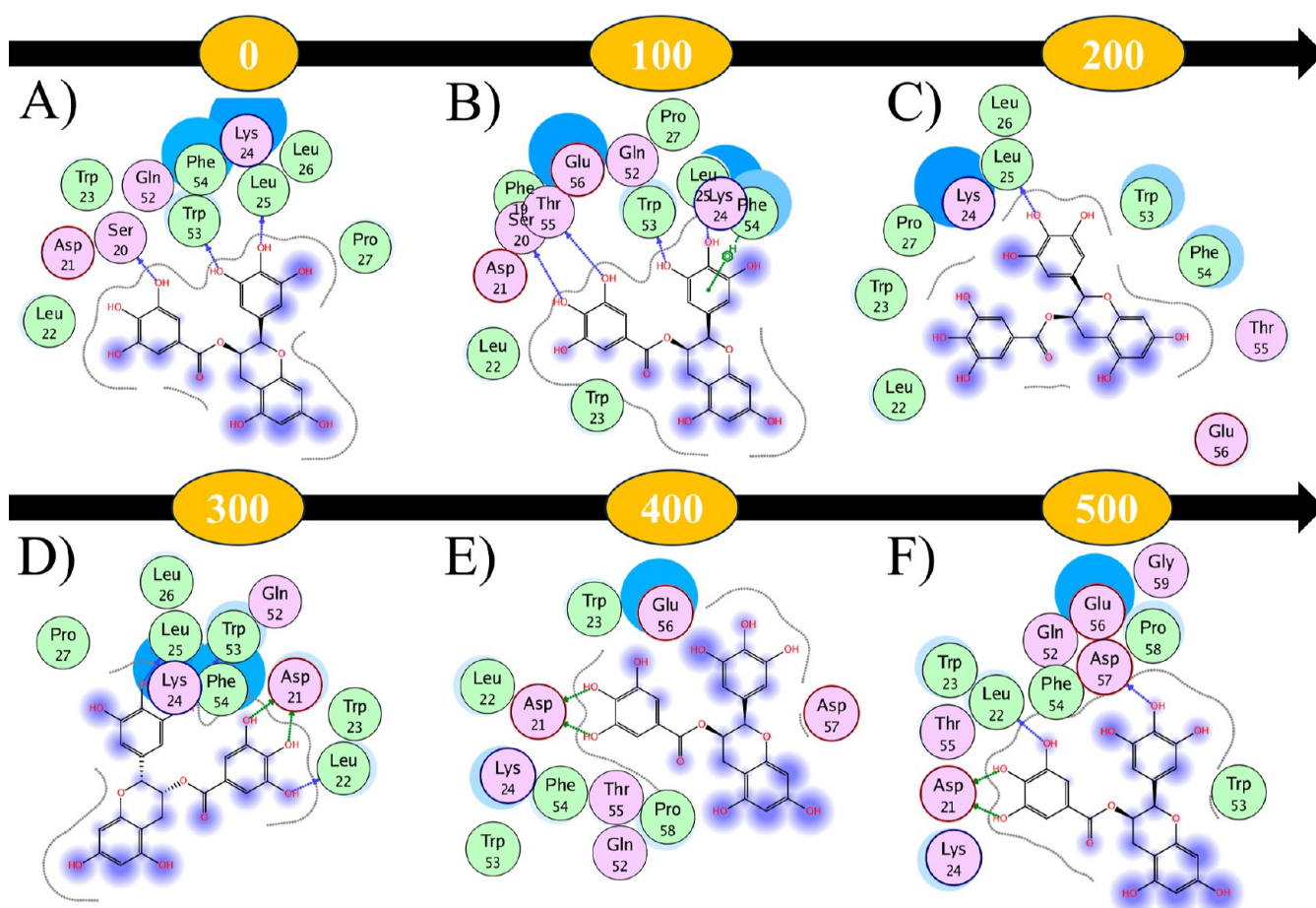
Figure 7. 2D representation of the R2−1 system at (A) 0, (B) 100, (C) 200, (D) 300, (E) 400, and (F) 500 ns.

Glu56, Asp57, and Pro58, whereas on the secondary cluster with Asp21, Leu22, Trp23, Lys24, Gln52, Trp53, Phe54, Thr55, and Glu56. In this way, the 500 ns simulation enhances ECGC interactions with the desired region from 4 (Trp23, Lys24, Gln52, and Trp53) to 6 found in both clusters: Trp23, Lys24, Gln52, Trp53, Phe54, and Thr55 (Movie 1B), further confirming the relevance of these residues seen within the per-residue energy decomposition (Table 5).

In this way, both structures did not dissociate during the 500 ns extended MD simulation. Both systems exhibited a certain degree of stability, with R2−1 demonstrating a higher level of stability (Figure S2). Within MMGBSA R2−1, the desired regions significantly contribute to ECGC as expected. Finally, within the most significant clusters of each system, it was observed that R2−1 gained interactions within the desired region, in contrast to R1−3, which exhibited a loss of interactions (Figure 6). Therefore, even though within R1−3, ECGC found a favorable interaction with p53, the interactions seen do not go accordingly to previous reports.[40] However, the R2−1 system behaved in a similar way to what would be expected (Movie 1B).

3.8. EGCG-Induced Conformation of p53 in R2−1. Given the consistently favorable ECGC binding observed in the R2−1 systems across all analyses, which corroborates findings reported by Zhao et al,[40] in addition to the potential binding pocket between Trp23 and Trp53 identified initially in R2−1 (Figure 1D) and seen during both the 100 ns (Figure 4B) and 500 ns simulations (Figure 6B), we aimed to further analyze the persistence and characteristics of this binding pocket throughout

the entire 500 ns MD simulation. In this way, R2−1 systems were analyzed each for 100 ns. As depicted in Movie 1B, the two structural conformations suggested by the R_g (Figure S2) are evident throughout the 500 ns simulation. Moreover, during the initial 300 ns, ECGC remained firmly bound to the binding pocket, showing minimal movement (Movie 1B). However, around 350 ns, the complex underwent a significant change, resulting in a reshaping of the binding pocket (Movie 1B).

At the initiation of the simulation, ECGC exhibited interactions with specific residues, namely, Ser20, Asp21, Leu22, Trp23, Lys24, Leu25, Leu26, Pro27, Gln52, Trp53, and Phe54 (Figure 7A). These interactions stemmed from both pyrogallol motifs, particularly their hydroxide components (Figure 7A). Notably, both motifs were situated within cleavage sites between the regions of interest, with one cleavage primarily involving Lys24 and Trp53, and the other centered around Trp23 (Figures 7A and 8A). This underscores the relevance of the binding pocket detected initially, which was also key to ECGC binding in the initial p53-ligand simulation (Figures 1D and 4B).

The consistency of this pattern was evident throughout the initial 300 ns of the simulation, with the pyrogallol motifs consistently positioned at the same cleavage sites (Movie 1B, Figures 7A, and 8A), while the majority of interactions remained the same. Specifically, at the 100 ns mark, ECGC exhibited interactions with residues Phe19, Ser20, Asp21, Leu22, Trp23, Lys24, Leu25, Pro27, Gln52, Trp53, Phe54, Thr55, and Glu56 (Figure 7B). By the 200 ns checkpoint, ECGC interactions extended to include Leu22, Trp23, Lys24, Leu25, Leu26, Pro27,
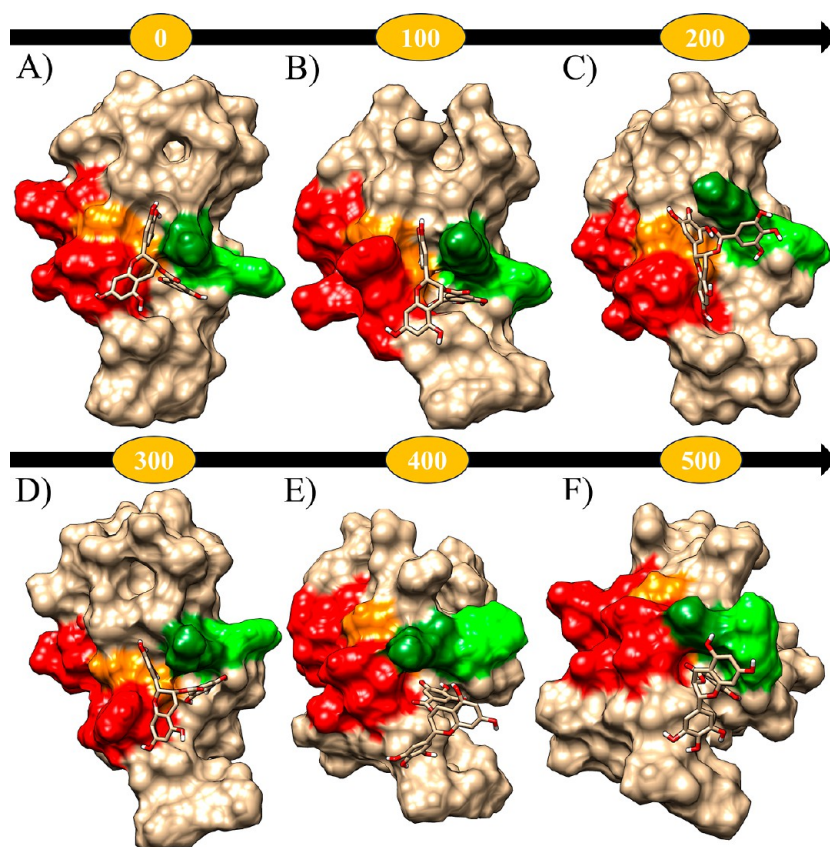
Figure 8. 3D representation of the R2−1 system at (A) 0, (B) 100, (C) 200, (D) 300, (E) 400, and (F) 500 ns. Color code: surface: Trp23−Lys24 is green, and Pro47−Thr55 is red. Trp23 is highlighted in light green, and Trp53 is shown in orange-red.

Trp53, Phe54, Thr55, and Glu56 (Figure 7C). Finally, at the 300 ns interval, prior to any notable conformational shifts, ECGC continued to engage with Asp21, Leu22, Trp23, Lys24, Leu25, Leu26, Pro27, Gln52, Trp53, and Phe54 (Figure 7D).

This is particularly relevant, not only as it behaves at it should be expected based to previous reports.[40] This analysis also highlights the relevance of the pyrogallol motifs on the binding of ECGC into p53′s NTD. These interactions also highlight the known inhibition of MDM2 binding as p53 interacted with MDM2 and MDMX through residues Phe19, Trp23, and Leu26.[77] Furthermore, it is noteworthy that throughout the 500 ns simulation, none of the regions of interest exhibited the formation of α-helices. This finding holds significance as α-helices are essential for binding proteins such as MDM2 and MDMX.[68−71] Therefore, the interaction of ECGC within R2−1, coupled with its structural conformation, strengthens its inhibitory effect and renders these sites inaccessible. This could potentially enhance inhibition of the p53−MDM2 interaction.

The conformational shift observed around 350 ns (Figure S2 and Movie 1B) is generated by the binding of Lys24 to the Pro47−Thr55 region (Figure 8E). During this shift, one of the pyrogallol motifs loses its binding interaction with Trp53, while the other retains these interactions, reminiscent of the initial conformation of R2−1 (Figure 1D). In this conformation, a plausible binding pocket is formed beneath Lys24, facilitating ligand interactions with Trp23 and Trp53 (Figures 7E and 8E). Furthermore, by 500 ns, this cleavage intensifies, allowing the pyrogallol motifs to re-establish interactions with a broader range of residues, including Asp21, Leu22, Trp23, Lys24, Gln52,

Trp53, Phe54, Thr55, Glu56, Asp57, Pro58, and Gly59 (Figures 7F and 8F). This mirrors most of the interactions observed during the initial 100 ns MD simulation, particularly those seen at the start of the simulation (Figure 3B), in which ECGC enhances that binding pocket as time progresses. Therefore, although ECGC may not fully regain the same position observed within the first 300 ns, it enhances the binding pocket from 400 to 500 ns, as seen in the initial 100 ns MD simulation (Figure 8E,F).

In summary, the first 300 ns witnessed remarkable stability in both pyrogallol motifs of EGCG across the regions of interest (Figure 8). The structure maintained consistent stability throughout this period, as evidenced by R_g analysis (Figure S2). Following a conformational shift around 350 ns, during which Lys24 bound to the Pro47−Thr55 region, one of the pyrogallol motifs sustained interactions with both Trp23 and Trp53, even during this change (Figures 7 and 8). This cleavage event resembled the plausible binding pocket observed in the initial conformation of R2−1 (Figure 1D). Notably, between 400 and 500 ns, ECGC demonstrated an enhancement of the binding pocket, reclaiming many of the interactions observed during the 500 ns MD simulation (Figures 7 and 8). Consequently, the binding pocket between Trp23 and Trp53 facilitated robust interactions with ECGC's pyrogallol motifs, enabling it to persistently engage with p53's NTD. This strong interaction with this particular region of p53 allows ECGC to block MDM2 and MDMX interactions by interacting with key residues and inducing a conformational shift that does not favor its binding. This finding unveils a potential mechanism by which EGCG exerts its therapeutic effects in cancer treatment.

3.9. EGCG Binding Pocket Perspectives. EGCG is not the only molecule capable of activating p53. Notably, significant strides have been made in the development of MDM2 and MDMX inhibitors.[78] However, despite these efforts, it has become evident that this approach falls short in achieving sustained suppression of tumor growth.[79] Nevertheless, recent advances in research have challenged the long-standing notion of p53 as an undruggable target. Novel molecules such as APR-246,[80] MANIO,[81] and CP-31398[82] have emerged, specifically designed to bind directly to p53 and enhance its stability. Despite this progress, to the best of our knowledge, no molecule has been shown to interact with the NTD region of p53. Moreover, the identified binding pocket around Trp23 and Trp53 holds promise.

On the one hand, the Trp23 region is pivotal in binding DM2 and MDMX.[69,70] Meanwhile, mutations of Trp53 and Phe54 have been demonstrated to enhance transactivation of p53, thereby contributing to its ability to suppress pancreatic cancer.[71] Furthermore, although the NTD region of p53 is a site for multiple protein interactions, EGCG binding does not appear to affect key p53 interactions. Instead, it has been found to increase phosphorylation of p53 at Ser15 and Ser20,[39] while also enhancing p53's anticancer activity.[35,83,84] Our research identified the pyrogallol motif as a key element in EGCG binding and conformational induction (Figures 7 and 8). Hence, these findings could serve as a foundation for solidifying EGCG's role as a p53 activator or uncovering novel molecules targeting this specific binding pocket.

4. CONCLUSIONS

Our study thoroughly explored the intricate dynamics governing the interaction between EGCG and the NTD of p53, with the aim to elucidate the underlying structural and thermodynamic basis for this binding phenomenon. Initially, a triplicate microsecond MD simulation was conducted to capture diverse p53 NTD conformations. Subsequently, the three most prevalent conformations from each simulation were meticulously analyzed. R2−1 stood out, exhibiting a distinct opening between the Trp23 and Trp53. This outcome is particularly intriguing as it represents the sole opening in the surface spanning Trp23−Lys24 and Pro47−Thr55, key residues that are known to interact with EGCG. Subsequently, all identified conformations underwent blind and target docking using four different software tools. Noteworthy interactions with both regions of interest were observed in R1−3, R2−1, R3−1, R3−2, and R3−3. Thus, all of these systems were chosen to perform a 100 ns simulation with EGCG. During further analysis, R1−3 and R2−1 stood out because they generated the highest stability, affinity, and interactions with the regions of interest. However, R2−1 was exceptional: it was the only system that enabled EGCG to interact with Trp23 and Trp53, resulting in an increased potential binding pocket within these crucial regions.

Notably, a structural analysis demonstrated that while not all key residues directly interacted with EGCG, most were integral components of its network of interactions. Furthermore, a dynamic visualization through a second 500 ns simulation revealed the pivotal role of the pyrogallol motifs on EGCG binding. This motif was found within two cleavages within the binding pocket. The first one was between Trp53 and Lys24, and the second was around Trp23. These cleavages facilitated sustained interactions throughout the simulation, the event when one of these regions drastically changes. In this way, the binding pocket found between Trp23 and Trp53 is instrumental

in enabling EGCG to impede p53 interactions, which may be related to the anticancer properties of EGCG.

■ ASSOCIATED CONTENT

ⓈI Supporting Information

The Supporting Information is available free of charge at https://pubs.acs.org/doi/10.1021/acsomega.3c10523.

rmsd and R_g of initial structures; molecular docking binding affinities; rmsd and R_g of R1−3 and R2−1 at 500 ns MD simulation; and 3D representation of the R2−1 system interactions at 20, 40, 60, 80, and 100 ns (PDF)

Visual representation of R1-3 and R2-1 systems throughout the 500 ns MD simulation (100 frames on Chimera software) [surface: Trp23−Lys24, green; Pro47−Thr55, red; Trp23, light green; and Trp53, orange-red] (MP4)

■ AUTHOR INFORMATION

Corresponding Author

Martiniano Bello − *Laboratorio de Diseño y Desarrollo de Nuevos Fármacos e Innovación Biotecnológica, Escuela Superior de Medicina, Instituto Politécnico Nacional, Ciudad de México 11340, Mexico;* ⊙ orcid.org/0000-0002-9686-0755; Email: bellomartini@gmail.com

Author

Erick Bahena Culhuac − *Laboratorio de Diseño y Desarrollo de Nuevos Fármacos e Innovación Biotecnológica, Escuela Superior de Medicina, Instituto Politécnico Nacional, Ciudad de México 11340, Mexico; Universidad Autónoma del Estado de México Facultad de Ciencias, Toluca 50000, Mexico*

Complete contact information is available at:
https://pubs.acs.org/10.1021/acsomega.3c10523

Notes

The authors declare no competing financial interest.

■ ACKNOWLEDGMENTS

■ REFERENCES

(1) Chen, L.; Zhang, H.-Y. Cancer Preventive Mechanismsof the Green Tea Polyphenol (−)-Epigallocatechin-3-Gallate. *Molecules* **2007**, *12* (5), 946−957.

(2) Fujiki, H.; Imai, K.; Nakachi, K.; Shimizu, M.; Moriwaki, H.; Suganuma, M. Challenging the Effectiveness of Green Tea in Primary and Tertiary Cancer Prevention. *J. Cancer Res. Clin. Oncol.* **2012**, *138* (8), 1259−1270.

(3) Johnson, R.; Bryant, S.; Huntley, A. L. Green Tea and Green Tea Catechin Extracts: An Overview of the Clinical Evidence. *Maturitas* **2012**, *73* (4), 280−287.

(4) Surh, Y.-J. Cancer Chemoprevention with Dietary Phytochemicals. *Nat. Rev. Cancer* **2003**, *3* (10), 768−780.

(5) Yang, C. S.; Wang, X. Green Tea and Cancer Prevention. *Nutr. Cancer* **2010**, *62* (7), 931−937.

(6) Singh, B. N.; Shankar, S.; Srivastava, R. K. Green Tea Catechin, Epigallocatechin-3-Gallate (EGCG): Mechanisms, Perspectives and Clinical Applications. *Biochem. Pharmacol.* **2011**, *82* (12), 1807−1821.

(7) Khan, N.; Afaq, F.; Saleem, M.; Ahmad, N.; Mukhtar, H. Targeting Multiple Signaling Pathways by Green Tea Polyphenol (−)-Epigallo-catechin-3-Gallate. *Cancer Res.* **2006**, *66* (5), 2500−2505.

(8) Yang, C. S.; Wang, H.; Li, G. X.; Yang, Z.; Guan, F.; Jin, H. Cancer Prevention by Tea: Evidence from Laboratory Studies. *Pharmacol. Res.* **2011**, *64* (2), 113−122.

(9) Levites, Y.; Amit, T.; Youdim, M. B. H.; Mandel, S. Involvement of Protein Kinase C Activation and Cell Survival/ Cell Cycle Genes in Green Tea Polyphenol (−)-Epigallocatechin 3-Gallate Neuroprotective Action. *J. Biol. Chem.* **2002**, *277* (34), 30574−30580.

(10) Relat, J.; Blancafort, A.; Oliveras, G.; Cufí, S.; Haro, D.; Marrero, P. F.; Puig, T. Different Fatty Acid Metabolism Effects of (−)-Epigallocatechin-3-Gallate and C75 in Adenocarcinoma Lung Cancer. *BMC Cancer* **2012**, *12* (1), 280.

(11) Sah, J. F.; Balasubramanian, S.; Eckert, R. L.; Rorke, E. A. Epigallocatechin-3-Gallate Inhibits Epidermal Growth Factor Receptor Signaling Pathway. *J. Biol. Chem.* **2004**, *279* (13), 12755−12762.

(12) Kanwar, J. Recent Advances on Tea Polyphenols. *Front. Biosci.* **2012**, *E4* (1), 111.

(13) Pianetti, S.; Guo, S.; Kavanagh, K. T.; Sonenshein, G. E. Green Tea Polyphenol Epigallocatechin-3 Gallate Inhibits Her-2/Neu Signaling, Proliferation, and Transformed Phenotype of Breast Cancer Cells. *Cancer Res.* **2002**, *62* (3), 652−655.

(14) Yang, F.; Oz, H.; Barve, S.; Devilliers, W.; Mcclain, C.; Varilek, G. The Green Tea Polyphenol, (−)-Epigallocatechin-3-Gallate Blocks Nuclear Factor-Kappa B Activation by Inhibiting IkappaB Kinase Activity in the Intestinal Epithelial Cell Line, IEC-6. *Gastroenterology* **2001**, *120* (5), A188.

(15) Chang, C.-M.; Chang, P.-Y.; Tu, M.-G.; Lu, C.-C.; Kuo, S.-C.; Amagaya, S.; Lee, C.-Y.; Jao, H.-Y.; Chen, M. Y.; Yang, J.-S. Epigallocatechin Gallate Sensitizes CAL-27 Human Oral Squamous Cell Carcinoma Cells to the Anti-Metastatic Effects of Gefitinib (Iressa) via Synergistic Suppression of Epidermal Growth Factor Receptor and Matrix Metalloproteinase-2. *Oncol. Rep.* **2012**, *28* (5), 1799−1807.

(16) Deng, Y.-T.; Lin, J.-K. EGCG Inhibits the Invasion of Highly Invasive CL1−5 Lung Cancer Cells through Suppressing MMP-2 Expression via JNK Signaling and Induces G2/M Arrest. *J. Agric. Food Chem.* **2011**, *59* (24), 13318−13327.

(17) Jung, Y. D.; Ellis, L. M. Inhibition of Tumour Invasion and Angiogenesis by Epigallocatechin Gallate (EGCG), a Major Component of Green Tea. *Int. J. Exp. Pathol.* **2001**, *82* (6), 309−316.

(18) Liu, L.-C.; Tsao, T. C.-Y.; Hsu, S.-R.; Wang, H.-C.; Tsai, T.-C.; Kao, J.-Y.; Way, T.-D. EGCG Inhibits Transforming Growth Factor-*β*-Mediated Epithelial-to-Mesenchymal Transition via the Inhibition of Smad2 and Erk1/2 Signaling Pathways in Nonsmall Cell Lung Cancer Cells. *J. Agric. Food Chem.* **2012**, *60* (39), 9863−9873.

(19) Singh, T.; Katiyar, S. K. Green Tea Catechins Reduce Invasive Potential of Human Melanoma Cells by Targeting COX-2, PGE2 Receptors and Epithelial-to-Mesenchymal Transition. *PLoS One* **2011**, *6* (10), No. e25224.

(20) DeLeo, A. B.; Jay, G.; Appella, E.; Dubois, G. C.; Law, L. W.; Old, L. J. Detection of a Transformation-Related Antigen in Chemically Induced Sarcomas and Other Transformed Cells of the Mouse. *Proc. Natl. Acad. Sci. U.S.A.* **1979**, *76* (5), 2420−2424.

(21) Rodier, F.; Campisi, J.; Bhaumik, D. Two Faces of P53: Aging and Tumor Suppression. *Nucleic Acids Res.* **2007**, *35* (22), 7475−7484.

(22) Teodoro, J. G.; Evans, S. K.; Green, M. R. Inhibition of Tumor Angiogenesis by P53: A New Role for the Guardian of the Genome. *J. Mol. Med.* **2007**, *85* (11), 1175−1186.

(23) Vazquez, A.; Bond, E. E.; Levine, A. J.; Bond, G. L. The Genetics of the P53 Pathway, Apoptosis and Cancer Therapy. *Nat. Rev. Drug Discovery* **2008**, *7* (12), 979−987.

(24) Vousden, K. H.; Lane, D. P. P53 in Health and Disease. *Nat. Rev. Mol. Cell Biol.* **2007**, *8* (4), 275−283.

(25) Levine, A. J. P53, the Cellular Gatekeeper for Growth and Division. *Cell* **1997**, *88* (3), 323−331.

(26) Campbell, H. G.; Mehta, R.; Neumann, A. A.; Rubio, C.; Baird, M.; Slatter, T. L.; Braithwaite, A. W. Activation of P53 Following Ionizing Radiation, but Not Other Stressors, Is Dependent on the Proline-Rich Domain (PRD). *Oncogene* **2013**, *32* (7), 827−836.

(27) Kastan, M. B.; Onyekwere, O.; Sidransky, D.; Vogelstein, B.; Craig, R. W. Participation of P53 Protein in the Cellular Response to DNA Damage. *Cancer Res.* **1991**, *51* (23 Pt 1), 6304−6311.

(28) Pustisek, N.; Situm, M. UV-Radiation, Apoptosis and Skin. *Coll. Antropol.* **2011**, *35* (2), 339−341.

(29) Bode, A. M.; Dong, Z. Post-Translational Modification of P53 in Tumorigenesis. *Nat. Rev. Cancer* **2004**, *4* (10), 793−805.

(30) Labuschagne, C. F.; Zani, F.; Vousden, K. H. Control of Metabolism by P53 - Cancer and Beyond. *Biochim. Biophys. Acta, Rev. Cancer* **2018**, *1870* (1), 32−42.

(31) Mihara, M.; Erster, S.; Zaika, A.; Petrenko, O.; Chittenden, T.; Pancoska, P.; Moll, U. M. P53 Has a Direct Apoptogenic Role at the Mitochondria. *Mol. Cell* **2003**, *11* (3), 577−590.

(32) Wang, P.; Reed, M.; Wang, Y.; Mayr, G.; Stenger, J. E.; Anderson, M. E.; Schwedes, J. F.; Tegtmeyer, P. P53 Domains: Structure, Oligomerization, and Transformation. *Mol. Cell. Biol.* **1994**, *14* (8), 5182−5191.

(33) Jeffrey, P. D.; Gorina, S.; Pavletich, N. P. Crystal Structure of the Tetramerization Domain of the P53 Tumor Suppressor at 1.7 Angstroms. *Science* **1995**, *267* (5203), 1498−1502.

(34) Inoue, T.; Stuart, J.; Leno, R.; Maki, C. G. Nuclear Import and Export Signals in Control of the P53-Related Protein P73. *J. Biol. Chem.* **2002**, *277* (17), 15053−15060.

(35) Amin, A. R. M. R.; Wang, D.; Zhang, H.; Peng, S.; Shin, H. J. C.; Brandes, J. C.; Tighiouart, M.; Khuri, F. R.; Chen, Z. G.; Shin, D. M. Enhanced Anti-Tumor Activity by the Combination of the Natural Compounds (−)-Epigallocatechin-3-Gallate and Luteolin. *J. Biol. Chem.* **2010**, *285* (45), 34557−34565.

(36) Hastak, K.; Gupta, S.; Ahmad, N.; Agarwal, M. K.; Agarwal, M. L.; Mukhtar, H. Role of P53 and NF-KB in Epigallocatechin-3-Gallate-Induced Apoptosis of LNCaP Cells. *Oncogene* **2003**, *22* (31), 4851−4859.

(37) Lee, M. H.; Han, D.-W.; Hyon, S.-H.; Park, J.-C. Apoptosis of Human Fibrosarcoma HT-1080 Cells by Epigallocatechin-3-O-Gallate via Induction of P53 and Caspases as Well as Suppression of Bcl-2 and Phosphorylated Nuclear Factor-KB. *Apoptosis* **2011**, *16* (1), 75−85.

(38) Qin, J.; Chen, H.-G.; Yan, Q.; Deng, M.; Liu, J.; Doerge, S.; Ma, W.; Dong, Z.; Wan-Cheng Li, D. Protein Phosphatase-2A Is a Target of Epigallocatechin-3-Gallate and Modulates P53-Bak Apoptotic Pathway. *Cancer Res.* **2008**, *68* (11), 4150−4162.

(39) Jin, L.; Li, C.; Xu, Y.; Wang, L.; Liu, J.; Wang, D.; Hong, C.; Jiang, Z.; Ma, Y.; Chen, Q.; Yu, F. Epigallocatechin Gallate Promotes P53 Accumulation and Activity via the Inhibition of MDM2-Mediated P53 Ubiquitination in Human Lung Cancer Cells. *Oncol. Rep.* **2013**, *29* (5), 1983−1990.

(40) Zhao, J.; Blayney, A.; Liu, X.; Gandy, L.; Jin, W.; Yan, L.; Ha, J.-H.; Canning, A. J.; Connelly, M.; Yang, C.; Liu, X.; Xiao, Y.; Cosgrove, M. S.; Solmaz, S. R.; Zhang, Y.; Ban, D.; Chen, J.; Loh, S. N.; Wang, C. EGCG Binds Intrinsically Disordered N-Terminal Domain of P53 and Disrupts P53-MDM2 Interaction. *Nat. Commun.* **2021**, *12* (1), 986.

(41) Baker, C. M.; Best, R. B. Insights into the Binding of Intrinsically Disordered Proteins from Molecular Dynamics Simulation. *Wiley Interdiscip. Rev. Comput. Mol. Sci.* **2014**, *4* (3), 182−198.

(42) Hirano, Y.; Okimoto, N.; Fujita, S.; Taiji, M. Molecular Dynamics Study of Conformational Changes of Tankyrase 2 Binding Subsites upon Ligand Binding. *ACS Omega* **2021**, *6* (27), 17609−17620.

(43) Ahmed, M.; Maldonado, A. M.; Durrant, J. D. From Byte to Bench to Bedside: Molecular Dynamics Simulations and Drug Discovery. *BMC Biol.* **2023**, *21* (1), 299.

(44) Kuzmanic, A.; Bowman, G. R.; Juarez-Jimenez, J.; Michel, J.; Gervasio, F. L. Investigating Cryptic Binding Sites by Molecular Dynamics Simulations. *Acc. Chem. Res.* **2020**, *53* (3), 654−661.

(45) Araki, M.; Matsumoto, S.; Bekker, G.-J.; Isaka, Y.; Sagae, Y.; Kamiya, N.; Okuno, Y. Exploring Ligand Binding Pathways on Proteins Using Hypersound-Accelerated Molecular Dynamics. *Nat. Commun.* **2021**, *12* (1), 2793.

(46) Herrera-Nieto, P.; Pérez, A.; De Fabritiis, G. Characterization of Partially Ordered States in the Intrinsically Disordered N-Terminal

Domain of P53 Using Millisecond Molecular Dynamics Simulations. *Sci. Rep.* **2020**, *10* (1), 12402.

(47) Case, D. A.; Cheatham, T. E.; Darden, T.; Gohlke, H.; Luo, R.; Merz, K. M.; Onufriev, A.; Simmerling, C.; Wang, B.; Woods, R. J. The Amber Biomolecular Simulation Programs. *J. Comput. Chem.* **2005**, *26* (16), 1668−1688.

(48) Wang, J.; Wolf, R. M.; Caldwell, J. W.; Kollman, P. A.; Case, D. A. Development and Testing of a General Amber Force Field. *J. Comput. Chem.* **2004**, *25* (9), 1157−1174.

(49) Jakalian, A.; Jack, D. B.; Bayly, C. I. Fast, efficient generation of high-quality atomic charges. AM1-BCC model: II. Parameterization and validation. *J. Comput. Chem.* **2002**, *23* (16), 1623−1641.

(50) Maier, J. A.; Martinez, C.; Kasavajhala, K.; Wickstrom, L.; Hauser, K. E.; Simmerling, C. Ff14SB: Improving the Accuracy of Protein Side Chain and Backbone Parameters from Ff99SB. *J. Chem. Theory Comput.* **2015**, *11* (8), 3696−3713.

(51) Ouyang, Y.; Zhao, L.; Zhang, Z. Characterization of the Structural Ensembles of P53 TAD2 by Molecular Dynamics Simulations with Different Force Fields. *Phys. Chem. Chem. Phys.* **2018**, *20* (13), 8676−8684.

(52) Jorgensen, W. L.; Chandrasekhar, J.; Madura, J. D.; Impey, R. W.; Klein, M. L. Comparison of Simple Potential Functions for Simulating Liquid Water. *J. Chem. Phys.* **1983**, *79* (2), 926−935.

(53) Darden, T.; York, D.; Pedersen, L. Particle mesh Ewald: An $N\cdot\log(N)$ method for Ewald sums in large systems. *J. Chem. Phys.* **1993**, *98* (12), 10089−10092.

(54) Ryckaert, J.-P.; Ciccotti, G.; Berendsen, H. J. C. Numerical Integration of the Cartesian Equations of Motion of a System with Constraints: Molecular Dynamics of n-Alkanes. *J. Comput. Phys.* **1977**, *23* (3), 327−341.

(55) DeLano, W. L. *The PyMOL Molecular Graphics System.* http://www.pymol.org/ 2002.

(56) Miller, B. R.; McGee, T. D.; Swails, J. M.; Homeyer, N.; Gohlke, H.; Roitberg, A. E. MMPBSA.Py: An Efficient Program for End-State Free Energy Calculations. *J. Chem. Theory Comput.* **2012**, *8* (9), 3314−3321.

(57) Feig, M.; Onufriev, A.; Lee, M. S.; Im, W.; Case, D. A.; Brooks, C. L. Performance Comparison of Generalized Born and Poisson Methods in the Calculation of Electrostatic Solvation Energies for Protein Structures. *J. Comput. Chem.* **2004**, *25* (2), 265−284.

(58) Bello, M. Binding Mechanism of Kinase Inhibitors to EGFR and T790M, L858R and L858R/T790M Mutants through Structural and Energetic Analysis. *Int. J. Biol. Macromol.* **2018**, *118*, 1948−1962.

(59) Kim, S.; Chen, J.; Cheng, T.; Gindulyte, A.; He, J.; He, S.; Li, Q.; Shoemaker, B. A.; Thiessen, P. A.; Yu, B.; Zaslavsky, L.; Zhang, J.; Bolton, E. E. PubChem 2019 Update: Improved Access to Chemical Data. *Nucleic Acids Res.* **2019**, *47* (D1), D1102−D1109.

(60) Hanwell, M. D.; Curtis, D. E.; Lonie, D. C.; Vandermeersch, T.; Zurek, E.; Hutchison, G. R. Avogadro: An Advanced Semantic Chemical Editor, Visualization, and Analysis Platform. *J. Cheminf.* **2012**, *4* (1), 17.

(61) Chemical Computing Group Inc.. *Molecular Operating Environment (MOE)*; Chemical Computing Group Inc., 2016; Vol. *1010*.

(62) Trott, O.; Olson, A. J. AutoDock Vina: Improving the Speed and Accuracy of Docking with a New Scoring Function, Efficient Optimization, and Multithreading. *J. Comput. Chem.* **2010**, *31* (2), 455−461.

(63) Morris, G. M.; Huey, R.; Lindstrom, W.; Sanner, M. F.; Belew, R. K.; Goodsell, D. S.; Olson, A. J. AutoDock4 and AutoDockTools4: Automated Docking with Selective Receptor Flexibility. *J. Comput. Chem.* **2009**, *30* (16), 2785−2791.

(64) Grosdidier, A.; Zoete, V.; Michielin, O. SwissDock, a Protein-Small Molecule Docking Web Service Based on EADock DSS. *Nucleic Acids Res.* **2011**, *39* (suppl), W270−W277.

(65) Pettersen, E. F.; Goddard, T. D.; Huang, C. C.; Couch, G. S.; Greenblatt, D. M.; Meng, E. C.; Ferrin, T. E. UCSF Chimera—A Visualization System for Exploratory Research and Analysis. *J. Comput. Chem.* **2004**, *25* (13), 1605−1612.

(66) Clementel, D.; Del Conte, A.; Monzon, A. M.; Camagni, G. F.; Minervini, G.; Piovesan, D.; Tosatto, S. C. E. RING 3.0: Fast Generation of Probabilistic Residue Interaction Networks from Structural Ensembles. *Nucleic Acids Res.* **2022**, *50* (W1), W651−W656.

(67) Smoot, M. E.; Ono, K.; Ruscheinski, J.; Wang, P.-L.; Ideker, T. Cytoscape 2.8: New Features for Data Integration and Network Visualization. *Bioinformatics* **2011**, *27* (3), 431−432.

(68) Wang, H.; Guo, M.; Wei, H.; Chen, Y. Targeting P53 Pathways: Mechanisms, Structures, and Advances in Therapy. *Signal Transduction Targeted Ther.* **2023**, *8* (1), 92.

(69) Kussie, P. H.; Gorina, S.; Marechal, V.; Elenbaas, B.; Moreau, J.; Levine, A. J.; Pavletich, N. P. Structure of the MDM2 Oncoprotein Bound to the P53 Tumor Suppressor Transactivation Domain. *Science* **1996**, *274* (5289), 948−953.

(70) Popowicz, G. M.; Czarna, A.; Rothweiler, U.; Szwagierczak, A.; Krajewski, M.; Weber, L.; Holak, T. A. Molecular Basis for the Inhibition of P53 by Mdmx. *Cell Cycle* **2007**, *6* (19), 2386−2392.

(71) Mello, S. S.; Valente, L. J.; Raj, N.; Seoane, J. A.; Flowers, B. M.; McClendon, J.; Bieging-Rolett, K. T.; Lee, J.; Ivanochko, D.; Kozak, M. M.; Chang, D. T.; Longacre, T. A.; Koong, A. C.; Arrowsmith, C. H.; Kim, S. K.; Vogel, H.; Wood, L. D.; Hruban, R. H.; Curtis, C.; Attardi, L. D. A P53 Super-Tumor Suppressor Reveals a Tumor Suppressive P53-Ptpn14-Yap Axis in Pancreatic Cancer. *Cancer Cell* **2017**, *32* (4), 460−473.e6. e6

(72) Dawson, R.; Müller, L.; Dehner, A.; Klein, C.; Kessler, H.; Buchner, J. The N-Terminal Domain of P53 Is Natively Unfolded. *J. Mol. Biol.* **2003**, *332* (5), 1131−1141.

(73) Chen, Y.-C. Beware of Docking! *Trends Pharmacol. Sci.* **2015**, *36* (2), 78−95.

(74) Kufareva, I.; Abagyan, R. Methods of Protein Structure Comparison. In *Homology Modeling: Methods and Protocols*; Springer, 2011; pp 231−257..

(75) Surti, M.; Patel, M.; Adnan, M.; Moin, A.; Ashraf, S. A.; Siddiqui, A. J.; Snoussi, M.; Deshpande, S.; Reddy, M. N. Ilimaquinone (Marine Sponge Metabolite) as a Novel Inhibitor of SARS-CoV-2 Key Target Proteins in Comparison with Suggested COVID-19 Drugs: Designing, Docking and Molecular Dynamics Simulation Study. *RSC Adv.* **2020**, *10* (62), 37707−37720.

(76) Becker, W.; Bhattiprolu, K. C.; Gubensäk, N.; Zangger, K. Investigating Protein-Ligand Interactions by Solution Nuclear Magnetic Resonance Spectroscopy. *ChemPhysChem* **2018**, *19* (8), 895−906.

(77) Joerger, A. C.; Fersht, A. R. The Tumor Suppressor P53: From Structures to Drug Discovery. *Cold Spring Harbor Perspect. Biol.* **2010**, *2* (6), a000919.

(78) Munisamy, M.; Mukherjee, N.; Thomas, L.; Pham, A. T.; Shakeri, A.; Zhao, Y.; Kolesar, J.; Rao, P. P. N.; Rangnekar, V. M.; Rao, M. Therapeutic Opportunities in Cancer Therapy: Targeting the P53-MDM2/MDMX Interactions. *Am. J. Cancer Res.* **2021**, *11* (12), 5762−5781.

(79) Alaseem, A. M. Advancements in MDM2 Inhibition: Clinical and Pre-Clinical Investigations of Combination Therapeutic Regimens. *Saudi Pharm. J.* **2023**, *31* (10), 101790.

(80) Zhang, Q.; Bykov, V. J. N.; Wiman, K. G.; Zawacka-Pankau, J. APR-246 Reactivates Mutant P53 by Targeting Cysteines 124 and 277. *Cell Death Dis.* **2018**, *9* (5), 439.

(81) Ramos, H.; Soares, M. I. L.; Silva, J.; Raimundo, L.; Calheiros, J.; Gomes, C.; Reis, F.; Monteiro, F. A.; Nunes, C.; Reis, S.; Bosco, B.; Piazza, S.; Domingues, L.; Chlapek, P.; Vlcek, P.; Fabian, P.; Rajado, A. T.; Carvalho, A. T. P.; Veselska, R.; Inga, A.; Pinho e Melo, T. M. V. D.; Saraiva, L. A Selective P53 Activator and Anticancer Agent to Improve Colorectal Cancer Therapy. *Cell Rep.* **2021**, *35* (2), 108982.

(82) Takimoto, R.; Wang, W.; Dicker, D. T.; Rastinejad, F.; Lyssikatos, J.; El-Deiry, W. S. The Mutant P53-Conformation Modifying Drug, CP-31398, Can Induce Apoptosis. *Cancer Biol. Ther.* **2002**, *1* (1), 47−55.

(83) Luo, K.-W.; Zhu, X.; Zhao, T.; Zhong, J.; Gao, H.; Luo, X.-L.; Huang, W.-R. EGCG Enhanced the Anti-Tumor Effect of Doxor-

ubicine in Bladder Cancer via NF-KB/MDM2/P53 Pathway. *Front. Cell Dev. Biol.* **2020**, *8*, 115197.

(84) Du, G.-J.; Zhang, Z.; Wen, X.-D.; Yu, C.; Calway, T.; Yuan, C.-S.; Wang, C.-Z. Epigallocatechin Gallate (EGCG) Is the Most Effective Cancer Chemopreventive Polyphenol in Green Tea. *Nutrients* **2012**, *4* (11), 1679−1691.